IN-SYNC II: VIRIAL STARS FROM SUB-VIRIAL CORES – THE VELOCITY DISPERSION OF EMBEDDED PRE-MAIN-SEQUENCE STARS IN NGC 1333

Jonathan B. Foster[1], Michiel Cottaar[2], Kevin R. Covey[3,4], Héctor G. Arce[5], Michael R. Meyer[2], David L. Nidever[6], Keivan G. Stassun[7,8], Jonathan C. Tan[9], S. Drew Chojnowski[10], Nicola da Rio[9], Kevin M. Flaherty[11], Luisa Rebull[12], Peter M. Frinchaboy[13], Steven R. Majewski[10], Michael Skrutskie[10], John C. Wilson[10], Gail Zasowski[14],

Submitted to ApJ

ABSTRACT

The initial velocity dispersion of newborn stars is a major unconstrained aspect of star formation theory. Using near-infrared spectra obtained with the APOGEE spectrograph, we show that the velocity dispersion of young (1-2 Myr) stars in NGC 1333 is 0.92 ± 0.12 km s^{-1} after correcting for measurement uncertainties and the effect of binaries. This velocity dispersion is consistent with the virial velocity of the region and the diffuse gas velocity dispersion, but significantly larger than the velocity dispersion of the dense, star-forming cores, which have a sub-virial velocity dispersion of 0.5 km^{-1}. Since the NGC 1333 cluster is dynamically young and deeply embedded, this measurement provides a strong constraint on the initial velocity dispersion of newly-formed stars. We propose that the difference in velocity dispersion between stars and dense cores may be due to the influence of a 70μG magnetic field acting on the dense cores, or be the signature of a cluster with initial sub-structure undergoing global collapse.

1. INTRODUCTION

The initial velocity of a newborn star is one of a few fundamental stellar properties set by the star-formation process; as such, it can provide powerful constraints on theories and simulations of star-formation. The 3D velocities of young stars can be assessed by measurements of radial velocities or proper motions, either of which allows an estimate of the stellar velocity dispersion as well as, in principle, global motions such as expansion/contraction and rotation. The radial velocities of young stars are particularly useful as these velocities can be directly compared to the (radial) velocity of the molecular gas in which they are embedded.

Previous work has shown that dense gas cores (both

[1] Yale Center for Astronomy and Astrophysics, Yale University, New Haven, CT 06520, USA; jonathan.b.foster@yale.edu
[2] Institute for Astronomy, ETH Zurich, Wolfgang-Pauli-Strasse 27, 8093 Zurich, Switzerland
[3] Lowell Observatory, Flagstaff, AZ 86001, USA
[4] Current Address: Dept. of Physics & Astronomy, Western Washington Univ., 516 High Street, Bellingham WA 98225, USA
[5] Department of Astronomy, Yale University, P.O. Box 208101, New Haven, CT 06520, USA
[6] Department of Astronomy, University of Michigan, Ann Arbor, MI 48109, USA
[7] Department of Physics & Astronomy, Vanderbilt University, VU Station B 1807, Nashville, TN, USA
[8] Physics Department, Fisk University, Nashville, TN 37208, USA
[9] Department of Astronomy, University of Florida, Gainesville, FL 32611, USA
[10] Department of Astronomy, University of Virginia, Charlottesville, VA 22904, USA
[11] Astronomy Department, Wesleyan University, Middletown, CT, 06459, USA
[12] Spitzer Science Center/Caltech, 1200 E. California Blvd., Pasadena, CA 91125, USA
[13] Department of Physics & Astronomy, Texas Christian University, Fort Worth, TX 76129, USA
[14] Department of Physics and Astronomy, Johns Hopkins University, Baltimore, MD 21218, USA

starless and hosting protostars) have a lower velocity dispersion than the diffuse gas in which they are embedded, and out of which these dense cores presumably formed (Walsh et al. 2004; André et al. 2007; Kirk et al. 2007; Rosolowsky et al. 2008; Kirk et al. 2010). In regions which form predominantly low-mass stars, the dense cores have a typical one-dimensional velocity dispersion of 0.4 to 0.5 km s^{-1}.

Studies of the radial velocity of stars in optically-revealed star-forming regions also find that the velocity dispersion of the stars is lower than the diffuse gas in the same region. For instance, in the Orion Nebula Cluster (ONC) and NGC 2264, the one-dimensional velocity dispersion of stars is 3-4 km s^{-1} (Fűrész et al. 2006, 2008; Tobin et al. 2009).

There are important distinctions between the young stellar velocities measured in the ONC and NGC 2264 and the dense gas core velocities in nearby low-mass regions. First, the ONC and NGC 2264 are significantly more massive and have a larger virial velocity dispersion. Second, the dynamical time in these regions is short, so although the stars are only 1-3 Myr old, their velocities may have evolved over 4-12 dynamical times (Tan et al. 2006). Finally, the fact that one is able to observe these stars in the optical suggests that they have significantly dispersed their natal gas, which can profoundly affect the stellar dynamics (e.g. Moeckel & Bate 2010). For these reasons the measurements in optically-revealed clusters do not directly reveal the initial velocity dispersion of new stars.

Covey et al. (2006) used near-infrared spectra of Class I and flat-spectrum objects within a number of nearby star-forming regions to show that these young stars have velocity dispersions similar to, or slightly larger than, the gas in which they are embedded. The velocity dispersions measured by Covey et al. (2006) were comparable to the 1.5 km s^{-1} radial velocity precision of their observations,

however, and thus provide only an upper limit on the true velocity dispersion of these protostars.

In a companion paper to this one, Cottaar et al. (2014a) show that the 2-6 Myr old, optically-revealed cluster IC 348 has a velocity dispersion of 0.6 - 0.7 km s^{-1}, which is slightly super-virial.

Simulations of the dynamical evolution of young clusters (e.g. Proszkow et al. 2009; Moeckel et al. 2012; Parker & Meyer 2012; Girichidis et al. 2012; Kruijssen et al. 2012) show that the cluster's initial conditions can be quickly erased by dynamical evolution. In Proszkow et al. (2009), for example, two simulations are compared, starting the stars with either a sub-virial or a virial velocity distribution. The sub-virial distribution collapses in size and increases its velocity dispersion within 1.5 Myr. Stars this young are normally still embedded, so near-infrared spectroscopy is necessary to measure their stellar properties and velocities.

Obtaining these high resolution near-infrared spectra is the goal of the INfrared Spectra of Young Nebulous Clusters (IN-SYNC) project (Cottaar et al. 2014b), which is measuring stellar velocities with a precision of ∼0.3 km s^{-1} for IC 348 (Cottaar et al. 2014a) and NGC 1333 in Perseus, as well as the more massive regions NGC 2264 and Orion A (Da Rio in prep.). IN-SYNC is an ancillary science program of the Apache Point Observatory Galactic Evolution Experiment (APOGEE; Zasowski et al. 2013; Majewski in prep.), part of the third Sloan Digital Sky Survey (SDSS-III; Gunn et al. 2006; Eisenstein et al. 2011).

The cluster NGC 1333 in Perseus presents us with an excellent location to compare the velocity dispersion of dense cores and young stars within a single region. NGC 1333 is young enough to contain both dense cores and young stars (∼ 1 Myr; Arnold et al. 2012, and references therein), near enough to resolve the dense gas cores (∼ 250 pc; Hirota et al. 2008; Bell et al. 2013; Plunkett et al. 2013), yet not so massive that the embedded pre-main sequence population is rendered inaccessible by dust extinction even in the near-infrared. NGC 1333 therefore affords us the opportunity to build a full picture of the velocities of the diffuse gas, the dense cores, and the young embedded stars within a single cluster.

2. OBSERVATIONS

2.1. Stellar Data

Spectra were obtained using the APOGEE multi-object spectrograph (Wilson et al. 2012). The details of the data reduction and spectral fitting are presented in Cottaar et al. (2014b). In brief, a grid of BT-Settl (Allard et al. 2012) model spectra are convolved to the resolution of the reduced IN-SYNC spectra. The main parameters that are allowed to vary in fitting to the models to the observed spectra are the effective temperature (T_{eff}), the veiling (r_H), the rotational velocity ($v \sin i$), the surface gravity ($\log(g)$) and the radial velocity (v_r) of the star. Initial parameter uncertainties are estimated from the Markov Chain Monte Carlo (MCMC) fitting process, although these uncertainties are then inflated to match the actual epoch-to-epoch variability seen in the parameters.

IN-SYNC targets in NGC 1333 were chosen from the Cores to Disks (c2d) Spitzer survey of Perseus (Jørgensen
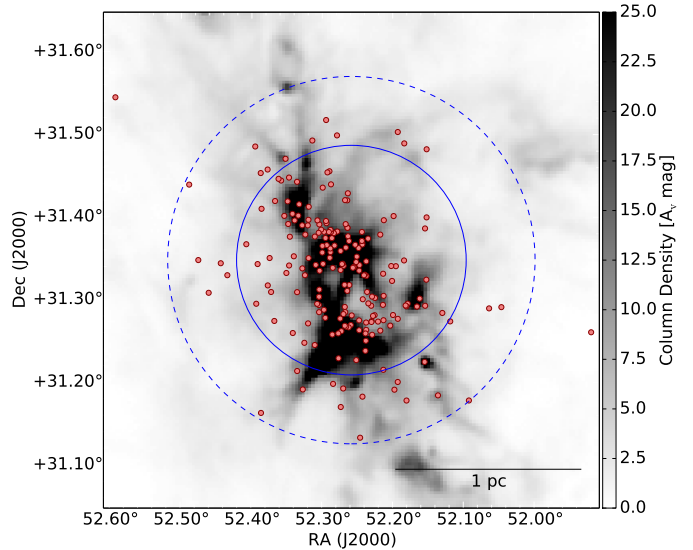
Fig. 1.— Column density map of NGC 1333 derived from *Herschel* data (grayscale). Red circles show the full IN-SYNC catalog. Fiducial radii are shown corresponding to the boundary of the dense gas (solid blue line) and the majority of stellar population (dashed blue line).
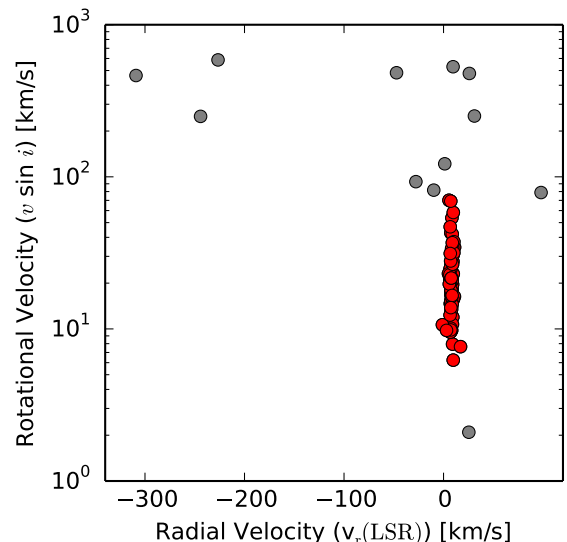
Fig. 2.— Radial velocity versus rotational velocity for the stars in NGC 1333 following the SNR and reduced χ^2 cuts described in subsection 2.4. The abrupt increase in radial velocity dispersion above 75 km s^{-1} corresponds to early-type stars with broad intrinsic line widths; the single star with $v \sin i < 5$ km s^{-1} is likely a field star. We keep only the intermediate stars (shown in red) for further analysis.

et al. 2006; Rebull et al. 2007), supplemented with focused surveys of NGC 1333 (Getman et al. 2002; Gutermuth et al. 2008; Winston et al. 2009, 2010) and candidate members selected based on their mid-IR variability from a preliminary analysis of the light curves obtained in NGC 1333 by the Spitzer YSOVAR program (Rebull et al. 2014).

Stars from all input surveys were given equal weight when assigning targets, and the primary selection crite-
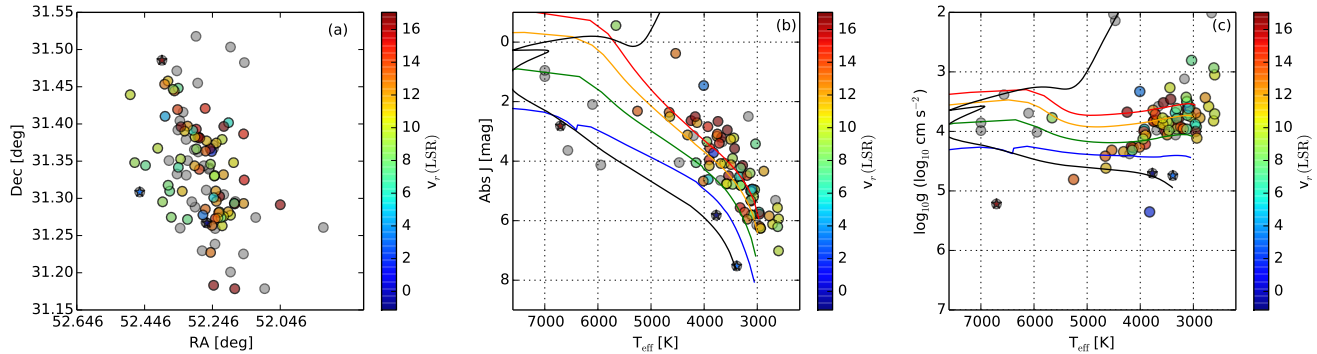
Fig. 3.— Sample of pre-main-sequence stars in NGC 1333 considered in this study. (a) The spatial distribution of stars, both included (color-coded by radial velocity) and not included (gray) in the sample based on the quality criteria given in the text. (b and c) Stars included and not included, with pre-main-sequence isochrones in color at 1 (red), 2 (orange), 6 (green) and 10 (blue) Myr and a 1 Gyr main-sequence isochrone (black); all isochrones from Dotter et al. (2008). The diagram of absolute J magnitude versus effective temperature shows a relatively tight clustering around 1-2 Myr, and is used to exclude non-cluster main-sequence stars (denoted with a star symbol) lying below the 10 Myr isochrone.

ria was H magnitude. Since the APOGEE spectrograph has a fiber collision limit of $71''$, we used three distinct plates in order to achieve nearly complete coverage of bright stars in the center of the cluster. We prioritized assigning fibers to stars with 7.5 mag $< H <$13.5 mag; this was limited at the faint end by signal-to-noise considerations and at the bright end by the potential for flux bleeding. Sources with $H<$ 12.5 magnitudes were considered highest priority targets, and then fainter sources were used to fill up a plate. A faint source that was selected for one plate was prioritized on subsequent plates so as to build up the signal-to-noise of faint stars.

This fiber assignment scheme ensured that only five 5 NGC 1333 candidate members with $H<$13.5 mag were not assigned a fiber on any of the NGC 1333 fiber plug plates. Otherwise, 141 likely NGC 1333 members with $H<$13.5 mag were assigned fibers on at least one NGC 1333 plate; of these, 107 were assigned fibers on two or more plates, with 79, 61, and 58 members assigned at least three, four or five fibers across both observing seasons. The observations are therefore close to complete for the bright stars in NGC 1333, but are significantly incomplete at fainter magnitudes, and biased against faint stars in the densest portions of the cluster.

These magnitude limits do not correspond to simple limits on stellar mass, as the intrinsic H-band luminosity of a star in NGC 1333 may significantly effected by extinction, either local (the envelope around a very young star) or global (from substructure within the dust and gas in the cluster as a whole). The former constraint limits the IN-SYNC sample to relatively older stars. Thus, the vast majority of IN-SYNC stars with a Gutermuth et al. (2008) classification from Spitzer are Class II, rather than Class I stars, simply because local extinction around Class I stars renders them very faint in H. For the typical 1 Myr old star in the sample, the H-band magnitude limit of 13.5 corresponds to roughly 0.1 $M_\odot$(see subsection 2.4).

IN-SYNC observations of NGC 1333 include observations of stars in the "West-End" of Perseus well outside of NGC 1333. We use a minimal-spanning tree (MST; Gutermuth et al. 2009) on the positions of candidate protostars in the region to define a boundary for the cluster. This method shows a break in the cumulative distribu-

tion of span-length at 0.15 degrees, or 0.65 pc. Cutting the MST at this span length produces a cluster boundary that corresponds well to what a by-eye identification of the cluster would provide, and corresponds to all stars within the boundary of the box $51.8° <$ R.A. $< 52.5°$ and $31.15° <$ Dec. $< 31.6°$. Table 1 presents the full list of candidate members in NGC 1333 used in this survey, not all of which were observed.

2.2. Gas Data

To compare with our stellar velocities, we measure the velocity and velocity dispersion of the local gas with a combination of different tracers. These include the ^{12}CO (1-0) and ^{13}CO (1-0) transitions, which trace relatively low volume-density gas; we use the data from the COMPLETE Survey (Ridge et al. 2006). In addition, we use maps from higher critical density transitions in the central region of the cluster. These maps were obtained from the JCMT archive and include ^{12}CO, ^{13}CO, and $C^{18}O$ (3-2) from Curtis & Richer (2011). The velocities of dense cores within NGC 1333 are drawn from the N_2H^+(1-0) observations of continuum sources from Kirk et al. (2007).

2.3. Dust Column Density Map

We have used the publicly available (André et al. 2010) Herschel data for NGC 1333 to construct a map of the dust column density over NGC 1333. This map was created from fitting the Herschel 160 - 500μm data with a single temperature modified black-body where the dust opacities at each wavelength are given by the opacities in Ossenkopf & Henning (1994) for dust grains with thin ice mantles, rather than assuming a simple power-law modification of the blackbody spectrum (i.e., taking a single value of β). Choosing instead to use β=2, normalized at 230 GHz (a typical assumption, see Schnee et al. 2010) produces a dust mass that is 10% greater. For the Ossenkopf & Henning (1994) model the opacity at 500 μm κ_{500} is 0.05 cm^2 g^{-1}; we assume a gas-to-dust ratio 100:1.

To account for large-scale gradients present in the Herschel data, the zero-point of this map was set by matching the column densities obtained around the edges of NGC 1333 with the COMPLETE (Ridge et al. 2006) ex-

tinction map based on 2MASS photometry. The COM-PLETE extinction map is lower resolution than our new *Herschel* column density map (2.5′ versus 36″), missing structure evident in the *Herschel* column density map. Additionally, the extinction map is also significantly biased at the position of the cluster by the presence of many embedded red stars. The *Herschel* dust column density map, anchored by the reliable (i.e., non-cluster) portions of the extinction map, therefore provides the best available tracer of the dust (and therefore gas) mass in NGC 1333. For comparison, the total mass of the cluster gas is 20% lower when estimated from the COMPLETE extinction map rather than the *Herschel*-derived column density map.

The column density map derived from *Herschel* is shown in Figure 1 along with all the stars in the IN-SYNC target catalog; the stars observed by IN-SYNC are a subset of these objects.

2.4. *Selecting a Sample of Stars for Analysis*

Table 2 shows the best-fit stellar parameters for all APOGEE spectra obtained in NGC 1333. For this analysis we have applied quality criteria to these fits. Specifically, we exclude all spectra with a S/N < 20, and stars for which the reduced χ^2 of the best model fit was > 10, as these spectra lead to unreliable parameter determinations.

We then trim stars with very low or high rotational velocity ($v \sin i < 5$ km s^{-1} or $v \sin i > 75$ km s^{-1}). The former cut removes only one star, 2M03291184+3121557, which is near the edge of the cluster and has a velocity far from the cluster mean; this is likely a contaminating field star. The latter cut may remove genuine cluster members, typically very early type stars dominated by hydrogen lines. The large $v \sin i$ for these stars means that they have broad absorption lines; these broad lines mean that the precision of the radial velocity fit is low, and therefore the stars exhibit a much broader spread in radial velocity than stars with more secure fits (see the abrupt increase in velocity spread in Figure 2).

These cuts on $v \sin i$ are similar to the cuts applied in Cottaar et al. (2014a) except that we adopt an upper limit of $v \sin i = 75$ km s^{-1} rather than 150 km s^{-1}, as this corresponds to the observed $v \sin i$ threshold for dramatically increased radial velocity scatter in NGC 1333. The poor radial velocity fits for these hot early-type stars means that we are unable to make any conclusive statements about the velocity dispersion at the high mass/effective temperature end of the distribution. Using the Dotter et al. (2008) pre-main-sequence isochrones and an age of 1 Myr (see Figure 3), this cut effectively corresponds to removing all stars with M $\gtrsim 3.5\ M_\odot$.

We remove all stars from the sample with a radial velocity uncertainty greater than 1.1 km s^{-1}, as these stars contribute little information about the velocity dispersion. We also remove stars with strong radial velocity variability. We estimate this in the same manner as Cottaar et al. (2014a), by calculating the χ^2 statistic for the model of constant radial velocity as

$$\chi^2 = \sum_i \frac{(v_i - \mu)^2}{\sigma_i^2}, \qquad (1)$$

where v_i and σ_i are the best-fit radial velocity and associated uncertainty in each epoch, and μ is the uncertainty-weighted mean radial velocity. If the probability of obtaining at least this large a χ^2 is less than 10^{-4}, we flag the star as a radial velocity variable and exclude it from the following velocity analysis. 6% of stars are flagged as having variable radial velocities in this fashion.

Finally, after applying these cuts, there are three stars that lie closer to the main-sequence isochrone than the 1-2 Myr isochrone where most of the target clusters (see Figure 3b, where these three stars are shown with star symbols). These three stars (2M03290289+3116010, 2M03293476+3129081, and 2M03295048+3118305) are all candidate members, rather than confirmed young stars, are radial velocity outliers, and two of them lie on the outskirts of the cluster (Figure 3a); we therefore conclude that these three stars are most likely contaminating field stars, rather than genuine members of the cluster, and we exclude them from further analysis. This leaves 70 stars for the analysis of the cluster's velocity dispersion.

Table 3 shows the uncertainty-weighted mean parameters for all stars observed by IN-SYNC, along with how many spectra were used in the determination and a flag to indicate stars that were identified as having a variable radial velocity.

For comparison with the gas velocities, we have converted all stellar heliocentric radial velocities into the velocity frame of the gas data. This is the kinematical Local Standard-of-Rest (LSRK), defined as a solar motion of 20 km/s in the direction of α(J2000),δ(J2000) = (18:03:50.29, +30:00:16.8). No other velocity correction, such as correction for the gravitational redshift (Pasquini et al. 2011) or convective blueshift (Shporer & Brown 2011) has been applied. These corrections, which account for the difference between the velocity of the photosphere and the velocity of the center of mass of the star, are typically on the order of a few hundred m s^{-1} (although the convective blueshift is poorly constrained for young stars). From a comparison with literature results, Cottaar et al. (2014b) estimates that the systematic uncertainty in the absolute zero point of the IN-SYNC radial velocity system is on the order of 0.5 km s^{-1}.

From the Dotter et al. (2008) isochrones, and the age of the cluster (1-2 Myr) from Figure 3b, we can assign a mass to each star based on the effective temperature. The lowest mass calculated for the Dotter et al. (2008) isochrones is $0.1 M_\odot$ (corresponding to $T_{\rm eff} = 3000$ K), and we do not see many stars with temperatures far below this. The mass function (number of stars per unit mass) increases down to the $0.1 M_\odot$ limit, suggesting that we are reasonably sampling the masses down to 0.1 $M_\odot$. We are therefore sampling masses between $3.5 M_\odot$ and down to close to the hydrogen burning limit. We are not sensitive to the velocity distribution of brown dwarfs or early-type stars.

3. RESULTS

3.1. *Stellar Velocity Dispersion*

The determination of the intrinsic velocity dispersion of the young stellar population in NGC 1333 requires two main corrections. First, the radial velocities of the young stars have significant and non-uniform uncertainties. Second, the velocity distribution will be inflated by
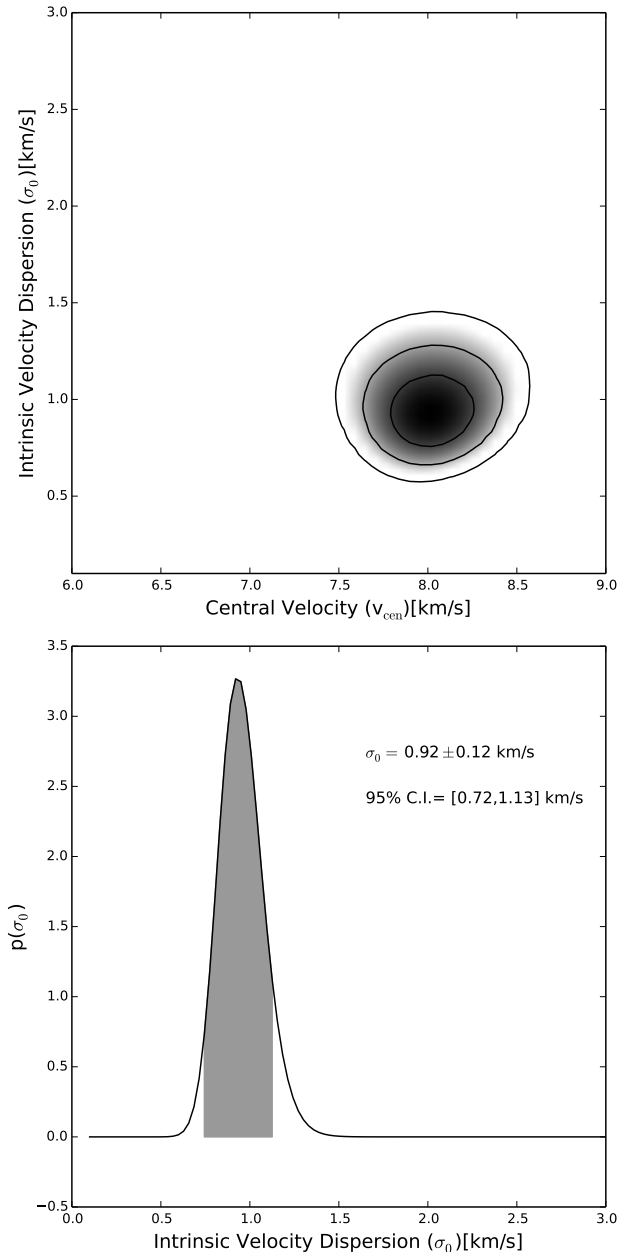
FIG. 4.— The inferred posterior probability distribution from VELBIN for NGC 1333, marginalized over the fraction of binaries (top) and marginalized over the fraction of binaries and the central velocity (bottom). Contours in the top panel show the 68%, 95%, and 99% credible intervals.

the presence of binaries, particularly close binaries. Multiple epochs of radial velocity data allow for the identification of some binaries, but not all, particularly since 40% of the stars in our NGC 1333 sample only have one observation meeting our SNR and goodness-of-fit criteria.

We take three distinct approaches to infer the intrinsic velocity dispersion: (1) use the VELBIN package (Cottaar & Hénault-Brunet 2014) to model the velocities at all epochs and the influence of binaries simultaneously, (2) use an outlier-resistant analytic estimate for the velocity dispersion in the case of non-uniform uncertainties, and (3) trim all stars with radial velocity uncertainty

greater than 0.5 km s^{-1} and use outlier-resistant estimates of the width of the distribution. Each of these approaches makes different assumptions, so it is important to check that they produce consistent estimates for the intrinsic velocity dispersion. For comparison, using just the sample standard deviation to estimate the width of the velocity distribution (i.e., ignoring errors and binary contamination) provides an estimate of 1.1±0.1 km s^{-1}.

We first infer the intrinsic velocity dispersion of NGC 1333 using the VELBIN package introduced in Cottaar & Hénault-Brunet (2014). This package generates a large sample of binary stars, with the mass ratio and orbital properties drawn from literature values. Specifically, we use the log-normal period distribution from Raghavan et al. (2010), the nearly-flat mass ratio distribution from Reggiani & Meyer (2013), and the flat eccentricity distribution from Duchêne & Kraus (2013). This distribution is then sampled and compared against the observed velocities and velocity errors from the real data set to infer the fraction of sources that are binaries and thus deduce the intrinsic velocity width of NGC 1333's stars after accounting for the influence of binaries. The underlying velocity distribution is assumed to be Gaussian, and so the posterior probability distribution function is inferred for the center of the velocity distribution, the intrinsic velocity dispersion, and the binary fraction.

Figure 4 shows the posterior probability distribution functions inferred for NGC 1333's velocity distribution, marginalized over the fraction of binaries (which is poorly constrained with a fairly flat posterior distribution between 20 and 70%) and over both the binary fraction and the central velocity. The latter posterior probability distribution for the intrinsic velocity dispersion, σ_0, is only slightly asymmetric, with a most likely value of 0.92±0.12 km s^{-1} and a 95% credible interval of [0.72, 1.13] km s^{-1}. The central velocity, v_{cen}, is 8.02 ±0.31 km s^{-1}. For comparison, the centroid velocity of the ^{13}CO (1-0) gas in this region ranges from 7 to 9 km s^{-1} (Quillen et al. 2005).

The correction for binarity is relatively small because we have data over a three-year baseline and have already removed 6% of the stars as radial-velocity variable (and thus likely binaries, see subsection 2.4). The remaining stars are known not to have a large radial velocity signature over the three years they were observed, and are therefore likely to either (1) not be in short-period binaries, or (2) not have an edge-on inclination that produces a large radial-velocity signature. Since we marginalize over all binary fractions in Figure 4, this estimate provides a conservative estimate for the intrinsic velocity dispersion, σ_0. If we fix the binary fraction at extreme values we get the following: for a binary fraction of 80%, σ_0=0.89±0.09 km s^{-1}; for a binary fraction of 20%, σ_0=0.98±0.10 km s^{-1}.

We also consider the effect of a period cut-off on the log-normal period distribution from Raghavan et al. (2010). This has a small influence since the inferred binary fraction increases/decreases in order to match the observational constraints. If the binary fraction is held fixed at 50%, then there is some sensitivity to adopting period cut-offs. We consider impose a cut-off on the maximum period. A semi-major cut-off of 1 AU provides an estimate of $\sigma_0 = 0.98±0.09$ km s^{-1}, a semi-major cut-off

of 10 AU gives $\sigma_0 = 0.89 \pm 0.10$ km s^{-1}, and a semi-major cut-off of 100 AU (or more) gives $\sigma_0 = 0.92 \pm 0.10$ km s^{-1}. This behavior is because the binaries that can most increase our observed velocity dispersion are binaries with intermediate periods – short-period binaries produce a large radial velocity signature which is easily ruled out by our multi-epoch observations while long-period binaries produce small radial velocity variations. All these variations are well within our uncertainty given for σ_0. Our estimate of σ_0 is therefore relatively robust against changes in the assumed binary population.

The second estimate for the velocity dispersion considers binaries as velocity outliers and infers the parameters of the velocity distribution using robust estimators. For this purpose we use the median and the inter-quartile range to infer the center and width of the distribution. A single velocity for each star is calculated as the weighted mean over all observed epochs, and a single velocity uncertainty is calculated as the median error across the epochs. This approach therefore uses less information than the VELBIN method.

To account for the non-uniform errors in the epoch-averaged radial velocity measurements, we adopt the outlier-resistant estimator given by Ivezić et al. (2014):

$$\sigma_0 = \sqrt{\zeta^2 \sigma_G^2 - e_{50}^2}, \qquad (2)$$

where σ_G is the unbiased estimator of σ for a Gaussian based on the interquartile range:

$$\sigma_G = 0.741(q_{75} - q_{25}) \qquad (3)$$

and

$$e_{50} = \mathrm{median}(e_i), \qquad (4)$$

$$\zeta = \frac{\mathrm{median}(\sigma_i)}{\mathrm{mean}(\sigma_i)}, \qquad (5)$$

and

$$\sigma_i = \sqrt{\sigma_G^2 + e_i^2 - e_{50}^2}, \qquad (6)$$

where the errors on individual stellar radial velocities are denoted as e_i. Uncertainties on this estimator are calculated from bootstrapping (Efron 1979). For the defined sample of stars in NGC 1333, this estimate of σ_0 is 1.04 $\pm$ 0.18 km s^{-1}. This broader confidence interval is indicative of the relative instability of this estimator for small samples (Ivezić et al. 2014).

Finally, based on the previous estimates of the intrinsic velocity dispersion, we trim all stars with radial velocity uncertainty > 0.5 km s^{-1}. This allows us to approximate the errors as roughly uniform (and small, compared to the intrinsic velocity dispersion) and simply calculate

$$\sigma_0 = \sqrt{\sigma_r^2 - e_{50}^2}, \qquad (7)$$

where σ_r is some robust estimator of the dispersion. Using either the Median Absolute Deviation (MAD Muller 2000) or σ_G for σ_r produces comparable results with σ_0 =1.12 $\pm$ 0.18 km s^{-1}. This estimate for the dispersion is actually slightly greater than the estimate just from the sample standard deviation of the untrimmed data, as many of the stars with radial velocity uncertainty between 0.5 and 1.1 km s^{-1} lie near average velocity. The

uncertainty on this estimate is again fairly large, because we have significantly reduced the amount of data used in this estimate. Note that Cottaar et al. (2014a) also trim all stars with radial velocity uncertainty > 0.5 km s^{-1} in their analysis of IC 348.

The estimates of the intrinsic velocity dispersion of the stars in NGC 1333 from VELBIN, the outlier-resistant analytic estimate, and the velocity dispersion of the error-trimmed subset are therefore all consistent with one another, within their relatively large uncertainties. We proceed with the VELBIN estimate of $\sigma_0 = 0.92 \pm 0.12$ km s^{-1}, as this estimate uses the most information.

3.2. Comparison with Low-Density Gas

Figure 5 shows the positions and velocities of the dense cores and IN-SYNC stars compared with the low-density gas tracer, ^{13}CO (1-0), which shows the general cloud gas. The cores and stars have similar, although not identical, spatial distributions. The cores have a small velocity dispersion (the one-dimensional velocity dispersion is 0.51 ± 0.05 km s^{-1}) and are strongly correlated with the highest intensity regions of the diffuse gas; this confirms what other studies have found – dense cores are not moving ballistically with respect to their surrounding diffuse gas (Walsh et al. 2004; Kirk et al. 2007, 2010).

The radial velocity errors on the stars would tend to diminish the appearance of any real correlation between the stellar velocities and that of the diffuse gas. Nonetheless, the structure of stars with low radial velocity errors reveals some cases where the stars are not well correlated with the diffuse gas. Comparing the radial velocity of the IN-SYNC stars with the first moment (i.e., the intensity-weighted mean) of the emission profile from the cloud gas (both ^{13}CO (1-0) and C^{18}O (3-2)) along the line of sight toward each of the stars shows no correlation between the diffuse gas velocity and the stellar velocity. This lack of a correlation arises because the first moment of the cloud gas is essentially the same at all locations in the cluster, while the stars have a broad spread in radial velocities.

Figure 6 displays the difference between stellar radial velocity and the centroid (1st moment) velocity of the ^{13}CO (1-0) and C^{18}O (3-2) gas. In both cases, the mean offset is close to zero, and the standard deviation of the offsets are roughly 1 km s^{-1}, which turns out to be comparable with the line-width of the ^{13}CO (1-0) gas.

3.3. Comparison of Stellar and Dense Core Velocity Dispersions

This measurement of the velocity dispersion in NGC 1333 represents the earliest measurement of this quantity[15]. NGC 1333 is still actively forming stars, with dense gas cores that are either starless or host to early (Class 0/I) protostars. These cores lie in roughly the same spatial area as the young stars measured by IN-SYNC but have a much tighter velocity dispersion. Taking only the cores from Kirk et al. (2007) that lie within our defined spatial boundary, the one-dimensional velocity dispersion is 0.51 ± 0.05 km s^{-1}.

---

[15] Arguably the stars in the ONC studied by Tobin et al. (2009) are of comparable age, but due to its higher mass, the dynamical age (i.e., age/dynamical time) of the ONC is significantly greater than the dynamical age of NGC 1333.
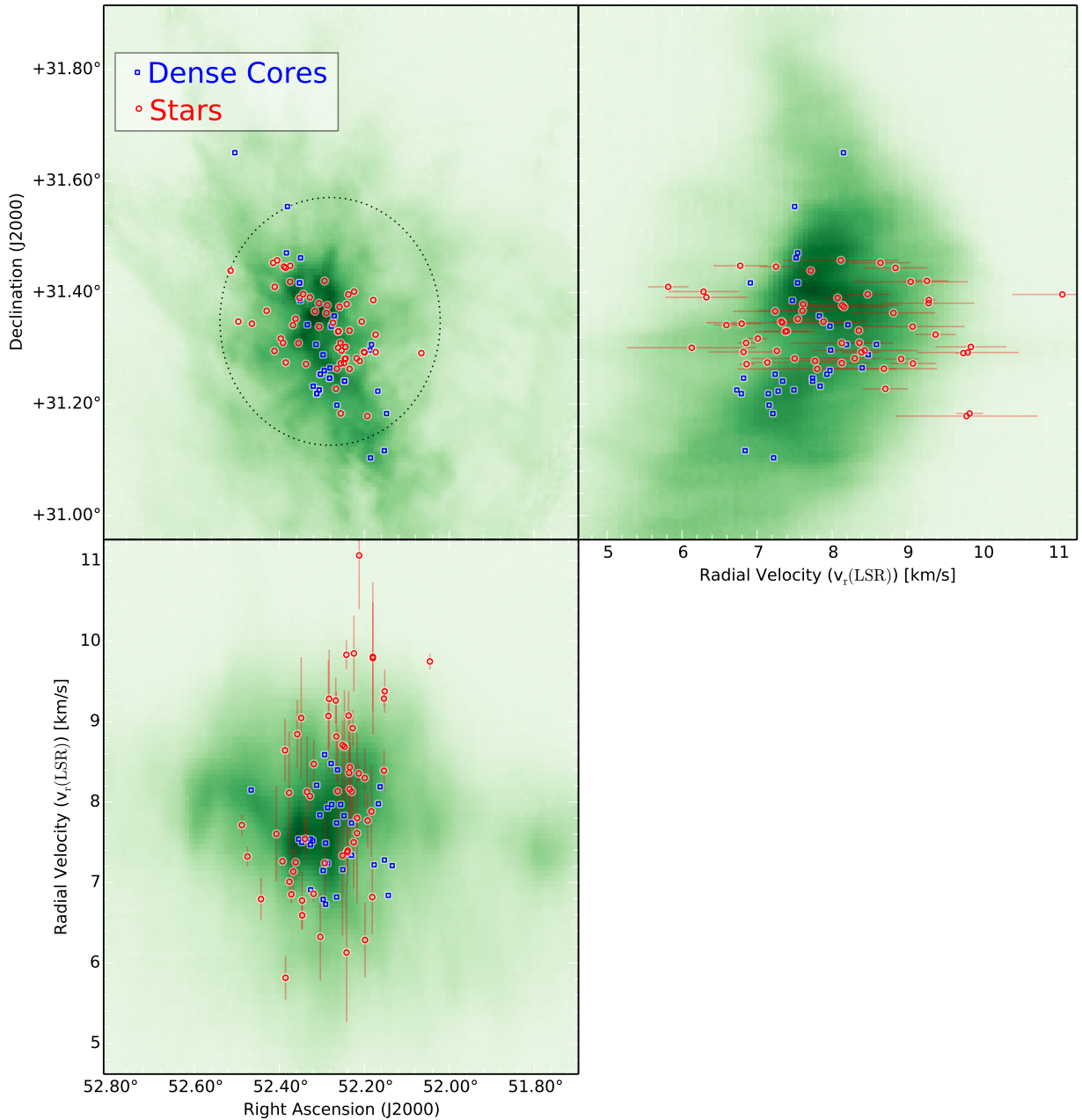
FIG. 5.— Positions and radial velocities of IN-SYNC stars (red) and N_2H^+ cores (blue; from Kirk et al. 2007) in NGC 1333. Shown in the green colorscale is the intensity of ^{13}CO (1-0) gas integrated over velocity (top-left), Right Ascension (top-right) and Declination (bottom-left). Error bars on the IN-SYNC stars show the 1σ uncertainty on radial velocity for these stars; the velocity uncertainty on the N_2H^+ cores is much smaller (typically < 0.05 km s^{-1}) and these errors are suppressed for clarity. The stellar population is contained within a radius of $800''(0.97$ pc), which is shown in the dotted circle (top-left).

Note that the determination of the dense core velocity dispersion is not corrected for the effects of binarity. One might imagine, for instance, that a binary system with separate accretion envelopes could produce a skewed line profile in N_2H^+. In the case of two envelopes with high relative velocities, the N_2H^+ line profile could separate into two velocity components, although this situation is indistinguishable from multiple widely-separated cores within the beam along the line of sight.

We can directly compare the velocity dispersion of the population of dense N_2H^+ cores and the population of stars observed with IN-SYNC. Because the two populations lie in similar positions within the cluster, this comparison is relating the velocity dispersion of stars just before they form (presumably stars inherit the systemic velocity of the dense cores out of which they form) and about 1-2 Myr after their birth.

Figure 7 shows the histograms of velocities for dense cores and stars. The distributions have consistent central velocities within their uncertainties (v_{cen}(cores) =
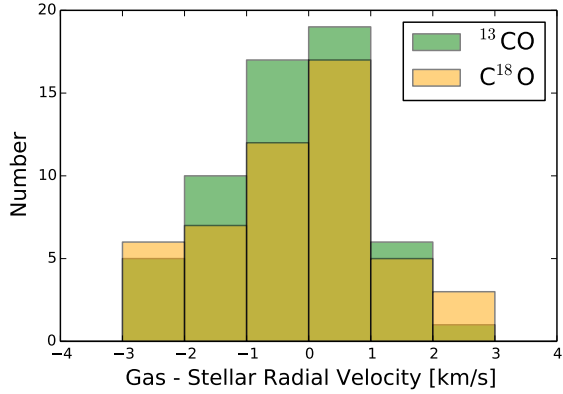
FIG. 6.— The velocity difference between each star's radial velocity and the centroid velocity of ^{13}CO (1-0) (green) and C^{18}O (3-2) (orange) at that position. Five stars fall outside the region covered by the C^{18}O (3-2) map and are not shown.

7.59 ± 0.09 km s^{-1}, $v_{\rm cen}$(stars) $= 8.02\pm0.31$ km s^{-1}). Because the stellar distribution appears broader due to the significant and non-uniform uncertainties on the radial velocity determinations, we plot the Gaussian distributions inferred in subsection 3.1 as well as the simple fit to the velocity distribution. The dense core velocity dispersion is significantly less broad than the stellar velocity dispersion inferred with VELBIN. The dense cores have a similar velocity dispersion to the line-width seen in the dense gas tracer (C^{18}O (3-2)), but significantly smaller dispersion than the diffuse gas (C^{13}O (1-0)).

3.4. Virial State of Stars and Cores

The full virial equation for a molecular cloud is

$$\frac{1}{2}\ddot{I} = 2(\mathcal{T} - \mathcal{T}_{\mathcal{S}}) + \mathcal{M} + \mathcal{W}, \qquad (8)$$

where $\ddot{I}$ denotes the acceleration of the expansion/contraction of the cloud, $\mathcal{T}$ is the kinetic energy of particles and gas within the cloud, $\mathcal{T}_{\mathcal{S}}$ is the surface term (surface pressure), $\mathcal{M}$ is the energy in the magnetic field and $\mathcal{W}$ is the gravitational potential energy. A simple virial analysis normally assumes that one can neglect the surface term and the magnetic field, and that a cloud's expansion or contraction is not accelerating ($\ddot{I} = 0$) so that

$$-\mathcal{W} = 2\mathcal{T}. \qquad (9)$$

Solving this equation for a spherical distribution with a power-law density distribution, $\rho(r) \propto r^{-k}$, gives (see Bertoldi & McKee 1992) a virial velocity dispersion, $\sigma_{\rm vir}$, via

$$\sigma_{\rm vir} = \sqrt{\frac{aMG}{5R}} \qquad (10)$$

where R is the radius, M the mass of the region under consideration, and a is a geometric factor of order unity:

$$a = \frac{1 - k/3}{1 - 2k/5}. \qquad (11)$$

Evaluating the virial state NGC 1333 therefore requires knowledge of the mass of the cluster at a given radius. This mass includes both the gas mass and the stellar mass. The projected gas distribution (Figure 1) shows
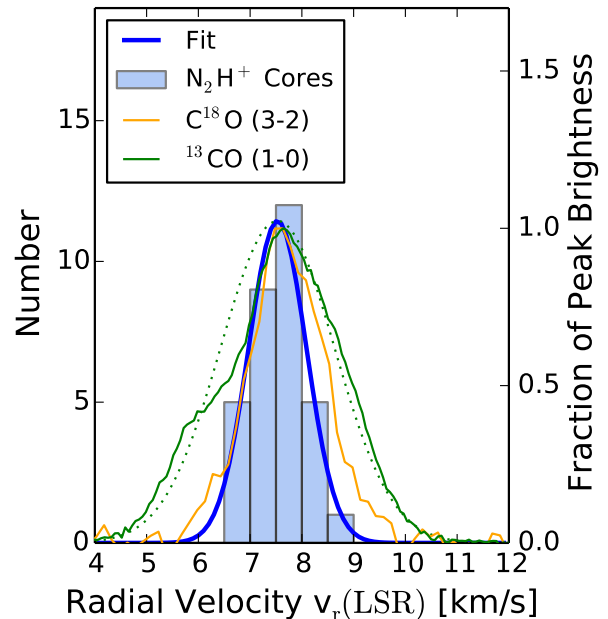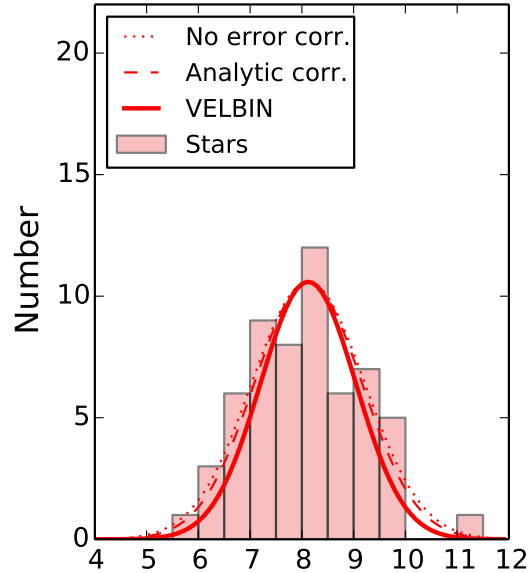
FIG. 7.— Comparison between the radial velocity distributions for N$_2$H$^+$ cores in NGC 1333 (bottom; from Kirk et al. 2007) and IN-SYNC stars (top). The stellar histogram is broadened by the errors on the radial velocity determination (which are negligible for the N$_2$H$^+$ cores). Lines show the inferred width without account for errors (dotted), VELBIN (solid) and the analytical correction for non-uniform errors given in the text (dashed). For comparison with the core velocity dispersion, the average spectrum of ^{13}CO (1-0) (green; low-density tracer) and C^{18}O (orange; high-density tracer) are over-plotted on the N$_2$H$^+$ core velocity distribution, scaled to the amplitude of the core velocity dispersion distribution. The dotted (green) line shows the line width of ^{13}CO (1-0) with $\sigma = 1.1$ km s^{-1} as estimated in subsection 3.4.

significant sub-structure and non-azimuthal symmetry, and so estimates of the virial velocity assuming a smooth distribution will necessarily be only a rough approximation.

We compare two estimates of the gas mass within NGC 1333. The first is the mass estimate derived from
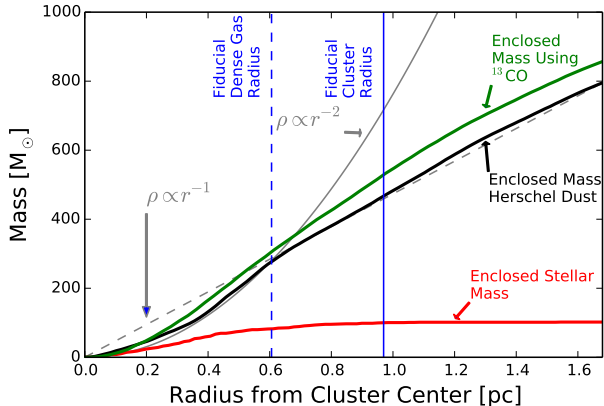
FIG. 8.— Mass enclosed within a given radius of the center of NGC 1333. Two different estimates are compared, that from CO (green) and that from the *Herschel* dust map (black). The enclosed mass profiles assuming a density power law $\rho \propto r^{-1}$ (constant column density) or $\rho \propto r^{-2}$ (normalized to the dust map at 1.65 pc and 0.6 pc, respectively) are shown in gray; the observed surface density profile is intermediate between these values. Also shown is the contribution from stars assuming that every star in the input IN-SYNC catalog has a mass of 0.5 $M_\odot$ (red line). Vertical lines denote radii of interest.

the *Herschel* column density map calculated in subsection 2.3. The second is using the COMPLETE ^{12}CO and ^{13}CO maps to derive the excitation temperature of the CO and then use the X-factors calculated for this region by Pineda et al. (2008) to convert the CO intensity to a total mass. The comparison between these two methods is shown in Figure 8. The conversion between CO and total mass depends on relations which were not calibrated in the central region of NGC 1333, since the extinction map used in the conversion was unreliable there (Pineda et al. 2008). For this reason, we use the mass estimated from the *Herschel* dust column density map, although the difference between the two profiles is not large.

Figure 8 also shows the enclosed mass for $\rho(r) \propto r^{-1}$ and $\rho(r) \propto r^{-2}$ profiles. The observed mass profile is intermediate between these two simple profiles, matching the $k = 1$ profile at radii > 0.6 pc, and close to the $k = 2$ profile at radii < 0.6 pc. This change in profile occurs at the edge of the region of high column density (i.e. ~ 15 mags of A_V) seen in the *Herschel* column density map (see Figure 1). The majority of the stellar population is contained with $800''(0.97$ pc at a distance of 250 pc), and we use this as the fiducial cluster radius.

IN-SYNC does not provide a complete census of all the stars in NGC 1333, so an estimate of the total stellar mass from these data requires significant extrapolation. Our input catalog contains 205 objects in the region considered. Low-mass regions such as this one have a typical mean stellar mass of 0.5 $M_\odot$. In order to show how this mass is distributed in Figure 8, we simply assign 0.5 $M_\odot$ to every star in the IN-SYNC catalog, giving a total mass of 102 $M_\odot$. For comparison, Lada et al. (1996) estimate a total stellar cluster mass of 45 $M_\odot$ over a similar region to that which is considered here. This is obviously a fairly rough approximation, but the stellar mass is much smaller than the gas mass, and therefore has relatively little influence on the virial velocity of the cluster.

The virial velocity given by Equation 10 can be evaluated as a function of radius. Since the projected mass

profile implies that the true density profile is between $\rho(r) \propto r^{-2}$ and $\rho(r) \propto r^{-1}$, we use a single value of $\rho(r) \propto r^{-1.5}$ to provide a continuous value for the virial velocity. This leads to a value of $a = 1.25$. We show the result of this calculation in gray in Figure 9, along with an estimate of the uncertainty, which is dominated by the systematic uncertainty on the mass estimate, which is a combination of an uncertain zero-point in our column density map, the uncertain dust emissivity, and our assumption of a single temperature component along the line of sight. We adopt a factor of two uncertainty on the mass to account for these sources of uncertainty. The virial velocity takes on a roughly constant value beyond 0.6 pc (as would be expected for the $\rho(r) \propto r^{-1}$ profile which is observed at large radii) of $\sigma_{\rm vir} = 0.79 \pm 0.20$ km s^{-1}.

Another estimate of the virial velocity comes from assuming that the diffuse gas is roughly in virial equilibrium, and therefore that the virial velocity dispersion of NGC 1333 can be estimated from the line width of the diffuse gas. As shown in Figure 7, the line profile for ^{13}CO (1-0) integrated over the cluster region is non-Gaussian. We adopt the common approach of measuring the FWHM of the emission and then converting to an (effective) σ for a Gaussian distribution. The result of measurement as a function of radius is shown in green in Figure 9. There are several important caveats with this measurement: the presence of significant outflow energy and momentum in NGC 1333 (e.g. Lefloch et al. 1998; Knee & Sandell 2000; Plunkett et al. 2013) means that the CO in NGC 1333 may be super-virial; on the other hand, ^{13}CO (1-0) may not be optically thin, so optical depth effects may increase the observed line width.

Finally, we can estimate the intrinsic velocity dispersion for both stars and dense cores, binned within a given radius. For this purpose we use VELBIN for the stars and the sample standard deviation for the cores (as we did in subsection 3.1 and subsection 3.1 for the full cluster). These measurements are displayed in Figure 9.

Figure 9 shows that the various estimates of the velocity dispersion approach constant values beyond about 0.4 pc. Inside this radius there is a suggestive dip in all measurements of the velocity dispersion, although for any individual tracer this is not a statistically significant decrease. At small radii, neglecting the surface term, $\mathcal{T}_S$, in Equation 8 is obviously incorrect since the surrounding mass at of the cluster gas makes a significant contribution. Furthermore, it is difficult to interpret the measured radial velocity of stars at radii smaller than the orbital radii. Therefore we take the velocity dispersions measured at large radii as indicative of the true state of the cluster.

The stellar velocity dispersion of 0.92 ± 0.12 km s^{-1} is therefore consistent with our estimate of the cluster's virial velocity (0.79 ± 0.20 km s^{-1}) and the line width of the surrounding diffuse gas (1.1 ± 0.1 km s^{-1}); the dense cores have a velocity dispersion of 0.51 ± 0.05 km s^{-1}, less than the velocity dispersion of the diffuse gas, and consistent with sub-virial.

4. DISCUSSION

4.1. *Sub-clusters in NGC 1333*

Lada et al. (1996) first noted the bimodal spatial dis-
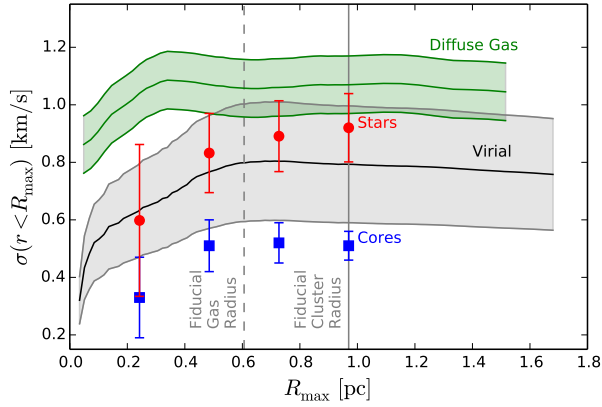
Fig. 9.— Velocity dispersion of the stars (red circles), dense cores (blue squares), diffuse gas (^{13}CO (1-0); green), and the expected velocity dispersion (black) if the cluster were in virial equilibrium (ignoring magnetic fields and external pressure). The velocity dispersions are shown as a function of R_{max}, and are calculated by considering all objects/positions interior to R_{max}. Vertical lines denote radii of interest. Shaded regions and error bars show estimates of the 1σ uncertainty of these values.

tribution of young stars in NGC 1333, which exhibits distinct northern and southern cluster in the stars observable in the near-infrared. The relatively unbiased survey of Gutermuth et al. (2008) confirmed the existence of these two sub-clusters, which can also be seen in Figure 3a as the clusters of stars around Declination 31°.37 and 31°.27, respectively. This clustering is less prominent in Figure 5 since the northern cluster contains fainter stars on average; fainter stars tend to have larger radial velocity uncertainties and are therefore suppressed in this figure.

Given the presence of sub-clusters, does it make sense to consider the velocity dispersion and virial velocity of the cluster as a whole? Using the Gutermuth et al. (2008) division of NGC 1333 into two clusters separated by a Declination of 31°.3, we use VELBIN to calculate the v_c and σ_0 for the northern and the southern clusters. For the northern cluster, $v_c = 7.9 \pm 0.42$ km s^{-1} and $\sigma_0 = 0.92 \pm 0.18$ km s^{-1}. For the southern cluster, $v_c = 8.1 \pm 0.40$ km s^{-1} and $\sigma_0 = 0.94 \pm 0.15$ km s^{-1}. There is thus no detectable kinematic difference between the two sub-clusters, and considering them separately produces roughly the same result for the stellar velocity dispersion. We therefore proceed with considering the velocity dispersion of the full cluster.

4.2. Velocity Gradients in NGC 1333

Quillen et al. (2005) report a velocity gradient in ^{13}CO (1-0) of 1 km s^{-1} in the north-south direction across NGC 1333. However, this gradient is fit in a larger region than we consider here, extending 15′ further south, and the magnitude of the gradient is strongly influenced by the substantial blue-shift in emission in the southern portion of their field. The diffuse gas shown in Figure 5 certainly displays some large-scale structure, but does not appear to exhibit a single consistent gradient. This is confirmed with higher-excitation CO lines; Bieging et al. (2014) present CO (2-1) and ^{13}CO (2-1) maps of NGC 1333 and speculate that the patchy variations in centroid velocity seen in these tracers could be ascribed

to a cloud-cloud collision.

We find no statistically significant velocity gradient in the stellar velocities across NGC 1333. For instance, considering just a north-south gradient, the best-fit velocity gradient across the region is -2.9 $\pm$ 2.2 km s^{-1} degree^{-1} (12.6 $\pm$ 9.6 km s^{-1} pc^{-1}). Since the area under consideration is 1/3 of a degree, the uncertainty on the magnitude of this gradient is on order of 0.7 km s^{-1}, leaving open the possibility of a gradient which is large enough to contribute to the observed spread in radial velocities seen in the region. Ultimately, we rely on the fact that we cover the same spatial region with our three tracers (diffuse gas, stars, and dense cores) and assume that any large-scale gradients or patchy structure effect the three tracers to a similar degree.

4.3. Comparison with Simulations

Proszkow et al. (2009) show that clusters which start with a sub-virial velocity distribution become slightly super-virial as the cluster collapses, while an initially virial velocity distribution remains roughly constant. Non-spherical elongation of the cluster, particularly along the line of sight, makes it difficult to distinguish between the case of sub-virial velocity dispersion and projection effects. Nonetheless, our results are broadly consistent with these simulations which start sub-virial, and then quickly become virial.

Offner et al. (2009) examined the velocity dispersion of young stars in a simulation of turbulent star formation. They find that star clusters forming in turbulent virialized clouds naturally begin with sub-virial velocity dispersions, however these sub-virial velocity dispersions persist for one free-fall time. The dynamical time, t_{dyn} = R/σ_{vir}, of NGC 1333 is 1.1 Myr, so our result is in conflict with this prediction. Furthermore, the stars in the Offner et al. (2009) simulation retain a strong correlation with the centroid velocity of the gas in which they are embedded; our stars show no such correlation. This simulation seems to predict the behavior of the starless and protostellar cores traced by N_2H^+, but not the behavior of the 1-2 Myr old stars that are observable in the near-infrared.

Both Kruijssen et al. (2012) and Girichidis et al. (2012) have recently studied the dynamical state of young stars in simulations. Kruijssen et al. (2012), in simulations with rather more mass than NGC 1333 (10^4 $M_{\odot}$ versus the 10^3 $M_{\odot}$ in NGC 1333), find that after one free-fall time most of the stars are in sub-clusters with relatively little gas left, and the stars are in viral equilibrium. Our study suggests that gas expulsion does not play a critical role in the virialization of young stars; the mass of NGC 1333 is still dominated by gas, and yet its young stars are virialized. Girichidis et al. (2012) study a slightly earlier stage, when only 20% of the mass is in protostars. In this study, only the central portions of the cluster are virialized, the external stars contribute to a sub-viral velocity distribution for the cluster as a whole. We see no evidence of this trend; the central regions and the outskirts of the cluster appear to have a similar viral state.

4.4. Explaining the Velocity Dispersion Difference

The difference between the 0.92 km s^{-1} stellar velocity dispersion and the 0.5 km s^{-1} dense core velocity dispersion can be explained in a number of ways. First, consider the additional terms in the virial equation that influence the gas and stars differently. After their formation, stars will cease to feel both the external pressure and the magnetic field. Since the dynamical time of NGC 1333 is 1.1 Myr, it is possible for the velocity dispersion of 1-2 Myr old stars to evolve subsequent to their formation.

We first consider the influence external pressure on the region. We can calculate the external pressure using the formula from Lada et al. (2008):

$$P_S = 4.5 \times 10^3 \phi_G k A_V^2, \tag{12}$$

where ϕ_G is a geometric factor of order 1 and A_V is the average column density in the region outside the cloud, which we can estimate as 2 mags of A_V for NGC 1333 from the COMPLETE extinction map. The energy due to surface pressure is simply

$$\mathcal{T}_\mathcal{S} = 4\pi R^3 P_S. \tag{13}$$

Our estimate for $\mathcal{T}_\mathcal{S}$ is therefore 1.3×10^{45} erg, which is less than 10% of the potential energy in the cluster ($|\mathcal{W}| = 3.3 \times 10^{46}$ erg). The external pressure does not seem to be significant.

We cannot estimate the strength of the magnetic field in NGC 1333 directly, but if we assume that the difference between the dense core kinetic energy and the energy of the potential well in which they are embedded comes purely from the magnetic field, then we can calculate the strength of that field as

$$\mathcal{M} = \frac{B^2 R^3}{6}, \tag{14}$$

which gives B = 66μG. This is a reasonable strength for the magnetic field in a region as dense as NGC 1333. Crutcher (2012) define an empirical relation between the strength of the magnetic field and the density of a region. For regions denser than the threshold particle density of $n_0 = 300$ cm^{-3},

$$B = B_0 \left(\frac{n}{n_0} \right)^{0.65} \tag{15}$$

where $B_0 = 10\mu$G. Assuming spherical symmetry, the particle density, n, of NGC 1333 is roughly 6×10^3 cm^{-3}, and thus $B = 70\mu$G.

Whether a magnetic field of this strength would actually provide support will depend at least partly on the field's morphology. In general, an ordered magnetic field will not provide support against collapse along magnetic field lines, but any realistic magnetic field configuration will involve turbulence translating support against collapse into all directions (see McKee & Ostriker 2007, and references therein). The exact details depend on how tangled the magnetic field is, and how much energy density is in large-scale field components; further investigation with simulations is required.

The diffuse gas has a broader velocity dispersion, and it might be expected to be more strongly influenced by the magnetic field. However, the diffuse gas could well be out of virial equilibrium due to the injection of energy from outflows from the existing young stars in NGC 1333.

It is therefore quite possible that NGC 1333 has a magnetic field strong enough to explain the dense cores' sub-virial motion. In this picture, the dense cores' velocities are constrained by the magnetic field; upon their formation the stars are freed from the magnetic field and evolve to the velocity dispersion dictated by gravity.

The most difficult problem with this explanation is that the young stellar population in NGC 1333 does not seem to be in the relaxed, centrally-condensed configuration expected for a virialized stellar population. As discussed in subsection 4.1, the stellar population exhibits significant structure in the form of two sub-clusters. Furthermore, an analysis of the radial density profile of the young stars in NGC 1333 by Gutermuth et al. (2008) finds a flat central surface density profile, which is interpreted as evidence of very little dynamical evolution.

We consider a second explanation: that the cluster NGC 1333 might be in a state of global collapse. The IN-SYNC stars, which are older than the current dense cores, therefore formed when the cluster was more extended than it is today, presumably with an initially sub-virial dispersion (like that possessed by the current dense cores). As the cluster globally collapsed, the potential energy of the stellar configuration was transformed into additional kinetic energy, rendering the stars dynamically hotter than the current population of dense cores. Cottaar et al. (2014a) have recently proposed that IC 348 is in a state of global collapse based on an independent line of reasoning. This explanation would therefore lend support to the idea that young clusters are generally in a state of global collapse.

In this picture the sub-virial velocity dispersion of dense cores can be explained if dense cores form at the convergent point of large-sale turbulent flows (Elmegreen 2007; Gong & Ostriker 2011) or if the cores form from a small number of velocity-coherent structures (perhaps filaments; Hacar & Tafalla 2011). The dense cores in NGC 1333 do exhibit coherence in position-velocity space (see top-right panel of Figure 5), so this is a reasonable explanation. If the IN-SYNC stars come from similarly sub-structured initial conditions, where those structures are now undergoing global collapse, then perhaps the stellar velocity dispersion could be inflated within the sub-structures before the sub-structure is erased. In this model it is unclear why the stellar sub-clusters in NGC 1333 have consistent central velocities; the naïve expectation in the case of global collapse is that they would have different bulk motions. Additional modeling of this point is required.

5. CONCLUSIONS

With the aid of the first high-resolution multi-object near-infrared spectrograph, APOGEE, we have measured, for the first time, the velocity dispersion of stars in an embedded young low-mass cluster where the stellar velocity dispersion can be directly compared with that of the dense star-forming cores and the diffuse gas in which both are embedded. Our results for NGC 1333 show that the 1-2 Myr old (Class II, where classification is possible) stars have an intrinsic velocity dispersion of 0.92 ± 0.12 km s^{-1} after correcting for measurement uncertainties and the influence of binaries. The velocity dispersion of

these young stars is significantly greater than the velocity dispersion of the dense cores (0.51 ± 0.05 km s^{-1}) in the same region.

Unlike for the dense cores, the stars studied here are moving ballistically with respect to the low density gas; there is no correlation between the two on a point-to-point comparison, although the mean velocity of the population is the same as the mean velocity of the diffuse gas and the width of the velocity distributions are similar. The stellar velocity dispersion is roughly virial, considering just the gravitational potential produced by the stars and gas in NGC 1333; in comparison the dense core velocity dispersion is sub-virial. Two possible (though not mutually exclusive or exhaustive) explanations for these results are (1) the presence of a magnetic field with strength of order 70μG having a strong influence on the velocity dispersion of the dense cores, or (2) a globally collapsing cluster with initial sub-structure. In both these scenarios, the velocity dispersion of the stars must increase quickly. Star-formation theories and simulations should strive to reproduce similar velocity dispersions for young stars roughly 1-2 Myr ($\sim$ 1-2 $t_{\rm dyn}$) after their birth.

6. ACKNOWLEDGEMENTS

REFERENCES

Allard, F., Homeier, D., & Freytag, B. 2012, Royal Society of London Philosophical Transactions Series A, 370, 2765 2.1

André, P., Belloche, A., Motte, F., & Peretto, N. 2007, A&A, 472, 519 1

André, P., Men'shchikov, A., Bontemps, S., et al. 2010, A&A, 518, L102 2.3

Arnold, L. A., Watson, D. M., Kim, K. H., et al. 2012, ApJS, 201, 12 1

Astropy Collaboration, Robitaille, T. P., Tollerud, E. J., et al. 2013, A&A, 558, A33 6

Bell, C. P. M., Naylor, T., Mayne, N. J., Jeffries, R. D., & Littlefair, S. P. 2013, MNRAS, 434, 806 1

Bertoldi, F., & McKee, C. F. 1992, ApJ, 395, 140 3.4

Bieging, J. H., Revelle, M., & Peters, W. L. 2014, ApJS, 214, 7 4.2

Cottaar, M., Covey, K., Foster, J., & et al. 2014a, Submitted 1, 2.4, 3.1, 4.4

Cottaar, M., & Hénault-Brunet, V. 2014, A&A, 562, A20 3.1

Cottaar, M., Covey, K. R., Meyer, M. R., et al. 2014b, ApJ, 794, 125 1, 2.1, 2.4

Covey, K. R., Greene, T. P., Doppmann, G. W., & Lada, C. J. 2006, AJ, 131, 512 1

Crutcher, R. M. 2012, ARA&A, 50, 29 4.4

Curtis, E. I., & Richer, J. S. 2011, MNRAS, 410, 75 2.2

Da Rio, N. in prep., in prep. 1

Dotter, A., Chaboyer, B., Jevremović, D., et al. 2008, ApJS, 178, 89 3, 2.4, 2.4

Duchêne, G., & Kraus, A. 2013, ARA&A, 51, 269 3.1

Efron, B. 1979, The Annals of Statistics, 7, 1 3.1

Eisenstein, D. J., Weinberg, D. H., Agol, E., et al. 2011, AJ, 142, 72 1

Elmegreen, B. G. 2007, ApJ, 668, 1064 4.4

Fűrész, G., Hartmann, L. W., Megeath, S. T., Szentgyorgyi, A. H., & Hamden, E. T. 2008, ApJ, 676, 1109 1

Fűrész, G., Hartmann, L. W., Szentgyorgyi, A. H., et al. 2006, ApJ, 648, 1090 1

Getman, K. V., Feigelson, E. D., Townsley, L., et al. 2002, ApJ, 575, 354 2.1

Girichidis, P., Federrath, C., Allison, R., Banerjee, R., & Klessen, R. S. 2012, MNRAS, 420, 3264 1, 4.3

Gong, H., & Ostriker, E. C. 2011, ApJ, 729, 120 4.4

Gunn, J. E., Siegmund, W. A., Mannery, E. J., et al. 2006, AJ, 131, 2332 1

Gutermuth, R. A., Megeath, S. T., Myers, P. C., et al. 2009, ApJS, 184, 18 2.1

Gutermuth, R. A., Myers, P. C., Megeath, S. T., et al. 2008, ApJ, 674, 336 2.1, 4.1, 4.4

Hacar, A., & Tafalla, M. 2011, A&A, 533, A34 4.4

Hirota, T., Bushimata, T., Choi, Y. K., et al. 2008, PASJ, 60, 37 1

Ivezić, Ž., Connolly, A., Vanderplas, J., & Gray, A. 2014,
    Statistics, Data Mining and Machine Learning in Astronomy
    (Princeton University Press) 3.1, 3.1
Jørgensen, J. K., Harvey, P. M., Evans, II, N. J., et al. 2006, ApJ,
    645, 1246 2.1
Kirk, H., Johnstone, D., & Tafalla, M. 2007, ApJ, 668, 1042 1,
    2.2, 3.2, 3.3, 5, 7
Kirk, H., Pineda, J. E., Johnstone, D., & Goodman, A. 2010,
    ApJ, 723, 457 1, 3.2
Knee, L. B. G., & Sandell, G. 2000, A&A, 361, 671 3.4
Kruijssen, J. M. D., Maschberger, T., Moeckel, N., et al. 2012,
    MNRAS, 419, 841 1, 4.3
Lada, C. J., Alves, J., & Lada, E. A. 1996, AJ, 111, 1964 3.4, 4.1
Lada, C. J., Muench, A. A., Rathborne, J., Alves, J. F., &
    Lombardi, M. 2008, ApJ, 672, 410 4.4
Lefloch, B., Castets, A., Cernicharo, J., Langer, W. D., & Zylka,
    R. 1998, A&A, 334, 269 3.4
Majewski, S. R. in prep., in prep. 1
McKee, C. F., & Ostriker, E. C. 2007, ARA&A, 45, 565 4.4
Moeckel, N., & Bate, M. R. 2010, MNRAS, 404, 721 1
Moeckel, N., Holland, C., Clarke, C. J., & Bonnell, I. A. 2012,
    MNRAS, 425, 450 1
Muller, J. 2000, Journal of Research of the National Institute of
    Standards and Technology, 105, 551 3.1
Offner, S. S. R., Klein, R. I., McKee, C. F., & Krumholz, M. R.
    2009, ApJ, 703, 131 4.3
Ossenkopf, V., & Henning, T. 1994, A&A, 291, 943 2.3
Parker, R. J., & Meyer, M. R. 2012, MNRAS, 427, 637 1
Pasquini, L., Melo, C., Chavero, C., et al. 2011, A&A, 526, A127
    2.4
Pineda, J. E., Caselli, P., & Goodman, A. A. 2008, ApJ, 679, 481
    3.4
Plunkett, A. L., Arce, H. G., Corder, S. A., et al. 2013, ApJ, 774,
    22 1, 3.4

Proszkow, E.-M., Adams, F. C., Hartmann, L. W., & Tobin, J. J.
    2009, ApJ, 697, 1020 1, 4.3
Quillen, A. C., Thorndike, S. L., Cunningham, A., et al. 2005,
    ApJ, 632, 941 3.1, 4.2
Raghavan, D., McAlister, H. A., Henry, T. J., et al. 2010, ApJS,
    190, 1 3.1
Rebull, L. M., Stapelfeldt, K. R., Evans, II, N. J., et al. 2007,
    ApJS, 171, 447 2.1
Rebull, L. M., Cody, A. M., Covey, K. R., et al. 2014, ArXiv
    e-prints, arXiv:1408.6756 2.1
Reggiani, M., & Meyer, M. R. 2013, A&A, 553, A124 3.1
Ridge, N. A., Di Francesco, J., Kirk, H., et al. 2006, AJ, 131,
    2921 2.2, 2.3
Rosolowsky, E. W., Pineda, J. E., Foster, J. B., et al. 2008, ApJS,
    175, 509 1
Schnee, S., Enoch, M., Noriega-Crespo, A., et al. 2010, ApJ, 708,
    127 2.3
Shporer, A., & Brown, T. 2011, ApJ, 733, 30 2.4
Tan, J. C., Krumholz, M. R., & McKee, C. F. 2006, ApJ, 641,
    L121 1
Tobin, J. J., Hartmann, L., Furesz, G., Mateo, M., & Megeath,
    S. T. 2009, ApJ, 697, 1103 1, 15
Walsh, A. J., Myers, P. C., & Burton, M. G. 2004, ApJ, 614, 194
    1, 3.2
Wilson, J. C., Hearty, F., Skrutskie, M. F., et al. 2012, in Society
    of Photo-Optical Instrumentation Engineers (SPIE) Conference
    Series, Vol. 8446, Society of Photo-Optical Instrumentation
    Engineers (SPIE) Conference Series 2.1
Winston, E., Megeath, S. T., Wolk, S. J., et al. 2009, AJ, 137,
    4777 2.1
—. 2010, AJ, 140, 266 2.1
Zasowski, G., Johnson, J. A., Frinchaboy, P. M., et al. 2013, AJ,
    146, 81 1

Foster, J.B. et al.

TABLE 1
Candidate young stars in NGC 1333

ObjID	2MASSID	RA [deg.]	Dec [deg.]	J [mag]	H [mag]	K [mag]
1	2M03274053+3115392	51.9189	31.2609	8.88	8.68	8.60
2	2M03281101+3117292	52.0459	31.2915	12.44	11.46	11.03
3	2M03281518+3117238	52.0633	31.2900	16.56	15.71	15.19
4	2M03282206+3110429	52.0919	31.1786	13.87	12.61	11.86
5	2M03282839+3116273	52.1183	31.2743	14.62	13.93	13.62
6	2M03283107+3117040	52.1295	31.2845	16.82	15.35	14.08
7	2M03283258+3111040	52.1357	31.1848	17.41	15.43	14.49
8	2M03283641+3128569	52.1517	31.4825	15.24	13.83	13.18
9	2M03283643+3124002	52.1518	31.4001	15.81	14.96	14.12
10	2M03283651+3119289	52.1522	31.3247	12.85	12.13	11.86
11	2M03283692+3117353	52.1538	31.2932	11.96	10.65	10.12
12	2M03283695+3123121	52.1540	31.3867	11.78	10.82	10.50
13	2M03283706+3113310	52.1545	31.2252	16.09	14.84	12.05
14	2M03283875+3118068	52.1616	31.3018	18.27	16.17	14.01
15	2M03283968+3117321	52.1654	31.2922	18.29	16.39	13.66
16	2M03283968+3117321	52.1654	31.2922	18.29	16.39	13.66
17	2M03284283+3117447	52.1785	31.2958	14.87	14.04	14.70
18	2M03284323+3110425	52.1802	31.1785	15.37	13.21	12.03
19	2M03284325+3117330	52.1803	31.2925	12.59	10.86	9.75
20	2M03284355+3117364	52.1815	31.2935	12.22	10.96	10.14
21	2M03284402+3129225	52.1835	31.4896	16.37	15.17	14.68
22	2M03284407+3120528	52.1837	31.3480	14.24	13.24	12.63
23	2M03284618+3116385	52.1925	31.2773	10.88	10.00	9.69
24	2M03284622+3112034	52.1926	31.2010	16.93	14.85	13.53
25	2M03284624+3130120	52.1927	31.5034	15.09	14.62	14.07
26	2M03284687+3120277	52.1953	31.3411	14.81	14.25	13.80
27	2M03284734+3111298	52.1973	31.1916	15.48	13.71	12.70
28	2M03284764+3124061	52.1985	31.4017	14.20	12.60	11.66
29	2M03284782+3116552	52.1993	31.2820	12.94	11.76	10.91
30	2M03284816+3119235	52.2007	31.3232	15.53	14.67	14.49
31	2M03284844+3120284	52.2019	31.3412	16.84	15.23	14.28
32	2M03284872+3116086	52.2032	31.2691	18.32	17.30	14.68
33	2M03285097+3123479	52.2124	31.3966	14.66	12.38	11.24
34	2M03285101+3118184	52.2126	31.3051	11.36	10.07	9.18
35	2M03285105+3116324	52.2128	31.2757	13.29	12.52	12.12
36	2M03285110+3112564	52.2130	31.2157	17.39	15.89	14.57
37	2M03285119+3119548	52.2133	31.3319	11.72	10.49	9.90
38	2M03285129+3117397	52.2136	31.2943	16.35	15.18	14.45
39	2M03285213+3115471	52.2173	31.2631	13.16	12.47	12.03
40	2M03285216+3122453	52.2174	31.3792	11.98	11.01	10.56
41	2M03285290+3116264	52.2205	31.2740	13.62	12.89	12.48
42	2M03285392+3118092	52.2248	31.3026	14.82	12.27	10.88
43	2M03285407+3116543	52.2254	31.2817	13.03	12.04	11.60
44	2M03285461+3116512	52.2276	31.2809	12.86	11.19	10.23
45	2M03285492+3115290	52.2289	31.2581	15.99	14.93	14.22
46	2M03285496+3118153	52.2290	31.3043	16.88	14.89	13.16
47	2M03285505+3116287	52.2295	31.2746	13.58	11.70	10.68
48	2M03285514+3116247	52.2298	31.2735	13.01	11.66	10.93
49	2M03285524+3117354	52.2302	31.2932	15.09	14.07	13.43
50	2M03285622+3117457	52.2343	31.2960	13.48	12.65	12.17
51	2M03285630+3122279	52.2347	31.3744	15.84	13.16	11.84
52	2M03285663+3118356	52.2360	31.3099	12.30	10.69	9.70
53	2M03285686+3119454	52.2369	31.3293	16.22	15.24	14.43
54	2M03285694+3120487	52.2373	31.3469	15.36	14.45	13.82
55	2M03285694+3115503	52.2373	31.2640	15.06	14.04	13.46
56	2M03285694+3116222	52.2374	31.2728	13.76	11.92	11.08
57	2M03285706+3115028	52.2378	31.2508	18.31	15.78	14.06
58	2M03285715+3115345	52.2382	31.2596	15.40	13.98	13.19
59	2M03285720+3114189	52.2384	31.2386	8.19	7.77	7.66
60	2M03285741+3119505	52.2392	31.3307	12.13	11.06	10.66
61	2M03285769+3119481	52.2404	31.3300	13.04	11.98	11.38
62	2M03285809+3118038	52.2421	31.3010	12.81	11.71	11.34
63	2M03285819+3110594	52.2425	31.1832	14.32	11.90	10.70
64	2M03285824+3122093	52.2427	31.3692	16.00	14.44	13.37
65	2M03285824+3122021	52.2428	31.3672	14.91	13.49	12.41
66	2M03285842+3122175	52.2434	31.3715	18.42	14.80	11.85
67	2M03285842+3122175	52.2434	31.3715	18.42	14.80	11.85
68	2M03285842+3122567	52.2434	31.3824	15.40	14.15	13.68
69	2M03285884+3108002	52.2457	31.1335	16.84	16.08	15.18
70	2M03285920+3120327	52.2468	31.3424	16.58	15.96	15.03
71	2M03285930+3115485	52.2472	31.2635	16.49	12.53	10.44
72	2M03285933+3120082	52.2472	31.3356	17.69	17.34	15.11
73	2M03285934+3116315	52.2473	31.2754	17.04	15.60	14.55
74	2M03285954+3121467	52.2482	31.3630	12.61	11.26	10.30

TABLE 1 — *Continued*

ObjID	2MASSID	RA [deg.]	Dec [deg.]	J [mag]	H [mag]	K [mag]
75	2M03290015+3121092	52.2506	31.3526	16.47	14.59	13.35
76	2M03290031+3113385	52.2513	31.2274	13.16	11.95	11.34
77	2M03290037+3120456	52.2516	31.3460	13.56	12.37	11.80
78	2M03290069+3122008	52.2529	31.3669	16.24	13.29	11.76
79	2M03290116+3120244	52.2549	31.3401	15.81	13.43	11.61
80	2M03290116+3120244	52.2549	31.3397	15.81	13.43	11.61
81	2M03290149+3120208	52.2562	31.3391	15.75	13.88	10.88
82	2M03290188+3116533	52.2578	31.2814	16.69	15.49	14.87
83	2M03290216+3116114	52.2590	31.2698	14.53	13.86	13.57
84	2M03290268+3119056	52.2612	31.3182	17.54	15.17	13.59
85	2M03290279+3122172	52.2617	31.3714	16.93	14.80	13.32
86	2M03290289+3116010	52.2620	31.2670	12.84	12.18	11.94
87	2M03290313+3122381	52.2631	31.3772	13.72	12.37	11.32
88	2M03290320+3125451	52.2634	31.4292	15.80	14.62	13.83
89	2M03290332+3123148	52.2639	31.3874	17.25	15.84	14.07
90	2M03290332+3123148	52.2639	31.3874	17.25	15.84	14.07
91	2M03290339+3118399	52.2642	31.3111	15.83	14.55	14.00
92	2M03290342+3125143	52.2643	31.4207	16.64	14.91	13.86
93	2M03290375+3116039	52.2657	31.2678	11.67	9.65	8.17
94	2M03290386+3121487	52.2661	31.3635	11.54	10.14	9.22
95	2M03290394+3123307	52.2665	31.3919	17.14	15.98	14.93
96	2M03290406+3117075	52.2669	31.2854	13.31	12.68	12.31
97	2M03290416+3125151	52.2674	31.4209	13.65	11.81	10.88
98	2M03290421+3116080	52.2675	31.2689	15.61	13.66	14.37
99	2M03290421+3117301	52.2676	31.2917	16.61	15.30	14.65
100	2M03290429+3119063	52.2679	31.3184	17.22	15.81	15.51
101	2M03290462+3120289	52.2693	31.3414	16.72	15.46	13.75
102	2M03290466+3116591	52.2695	31.2831	15.55	13.91	12.66
103	2M03290472+3111348	52.2697	31.1930	18.50	15.64	14.45
104	2M03290493+3120385	52.2706	31.3440	15.58	14.60	12.98
105	2M03290506+3120377	52.2716	31.3436	16.42	13.83	12.59
106	2M03290536+3115446	52.2724	31.2624	16.67	16.62	14.92
107	2M03290554+3110142	52.2731	31.1706	17.07	16.86	15.67
108	2M03290566+3120107	52.2736	31.3363	17.11	16.40	15.48
109	2M03290567+3121338	52.2736	31.3594	17.55	15.35	13.29
110	2M03290575+3116396	52.2741	31.2777	14.49	11.61	9.93
111	2M03290631+3113464	52.2764	31.2296	18.02	14.70	12.66
112	2M03290642+3115348	52.2768	31.2597	16.43	16.09	15.28
113	2M03290680+3122585	52.2784	31.3829	16.95	15.31	14.33
114	2M03290693+3129571	52.2789	31.4992	16.54	15.42	14.77
115	2M03290773+3121575	52.2822	31.3660	15.27	13.80	10.43
116	2M03290794+3122515	52.2832	31.3809	13.00	11.18	10.19
117	2M03290817+3111548	52.2840	31.1986	17.25	15.77	14.98
118	2M03290832+3120203	52.2847	31.3390	14.68	12.90	12.01
119	2M03290844+3115298	52.2852	31.2583	15.54	15.04	13.78
120	2M03290862+3122297	52.2859	31.3749	16.43	16.01	14.63
121	2M03290896+3126239	52.2874	31.4400	16.90	15.55	14.75
122	2M03290895+3122562	52.2874	31.3823	16.06	13.42	11.72
123	2M03290908+3123056	52.2879	31.3849	14.65	12.94	11.89
124	2M03290907+3121291	52.2879	31.3580	15.57	14.53	12.98
125	2M03290915+3121445	52.2881	31.3624	14.48	14.81	12.97
126	2M03290933+3121042	52.2889	31.3511	16.42	14.28	13.15
127	2M03290948+3127209	52.2895	31.4558	14.15	13.18	12.69
128	2M03290964+3122564	52.2902	31.3823	11.27	10.16	9.53
129	2M03291018+3127159	52.2924	31.4544	15.55	14.72	14.13
130	2M03291037+3121591	52.2932	31.3664	9.37	7.99	7.17
131	2M03291046+3123348	52.2936	31.3930	15.63	13.82	12.76
132	2M03291064+3123442	52.2943	31.3956	18.59	16.56	15.12
133	2M03291064+3131039	52.2944	31.5178	12.78	11.95	11.59
134	2M03291079+3122301	52.2950	31.3750	14.90	13.67	12.93
135	2M03291082+3116427	52.2952	31.2785	15.65	14.11	13.04
136	2M03291130+3117175	52.2971	31.2882	13.98	13.37	12.92
137	2M03291132+3122570	52.2972	31.3825	14.90	13.43	12.52
138	2M03291163+3120374	52.2985	31.3437	15.43	13.58	12.67
139	2M03291177+3126095	52.2991	31.4360	17.15	15.75	14.78
140	2M03291184+3121557	52.2994	31.3655	14.44	13.40	13.21
141	2M03291188+3121271	52.2995	31.3575	17.22	15.70	12.82
142	2M03291228+3123065	52.3012	31.3852	17.86	16.25	15.26
143	2M03291279+3120077	52.3033	31.3355	14.68	13.78	13.29
144	2M03291288+3118455	52.3037	31.3126	16.94	15.87	14.96
145	2M03291290+3123293	52.3038	31.3915	13.42	12.57	12.07
146	2M03291294+3117071	52.3040	31.2853	16.22	15.51	15.30
147	2M03291294+3118146	52.3040	31.3040	18.60	17.77	14.12
148	2M03291294+3118146	52.3040	31.3040	18.60	17.77	14.12
149	2M03291303+3117383	52.3043	31.2940	15.23	14.58	14.16

Foster, J.B. et al.

TABLE 1 — *Continued*

ObjID	2MASSID	RA [deg.]	Dec [deg.]	J [mag]	H [mag]	K [mag]
150	2M03291312+3122529	52.3047	31.3813	12.87	11.12	10.11
151	2M03291355+3123469	52.3065	31.3964	16.61	15.90	15.12
152	2M03291361+3117434	52.3067	31.2954	16.44	14.25	13.03
153	2M03291410+3120329	52.3088	31.3425	16.02	15.46	15.25
154	2M03291433+3114441	52.3100	31.2456	17.76	16.02	14.34
155	2M03291443+3122362	52.3101	31.3767	14.61	13.53	13.04
156	2M03291532+3129346	52.3139	31.4930	18.08	17.75	15.27
157	2M03291653+3124462	52.3189	31.4128	16.97	16.24	15.18
158	2M03291655+3121025	52.3190	31.3507	14.98	13.31	12.43
159	2M03291659+3123495	52.3192	31.3971	13.25	11.84	11.18
160	2M03291667+3116182	52.3196	31.2717	11.44	10.75	10.43
161	2M03291681+3123252	52.3201	31.3903	15.42	14.32	13.58
162	2M03291766+3122451	52.3237	31.3792	9.97	8.92	8.32
163	2M03291776+3119481	52.3241	31.3300	14.80	13.65	12.99
164	2M03291793+3114535	52.3247	31.2482	16.62	14.95	14.04
165	2M03291844+3111304	52.3269	31.1918	16.41	16.08	15.53
166	2M03291865+3120178	52.3278	31.3383	17.51	15.97	14.61
167	2M03291872+3123254	52.3281	31.3904	11.45	10.68	10.33
168	2M03291977+3124572	52.3324	31.4158	8.83	8.54	8.35
169	2M03292003+3124076	52.3336	31.4021	17.16	14.70	12.04
170	2M03292037+3112506	52.3349	31.2141	16.25	15.34	14.97
171	2M03292042+3118342	52.3352	31.3095	14.40	12.01	10.47
172	2M03292052+3126347	52.3355	31.4430	16.76	15.34	14.73
173	2M03292130+3123464	52.3388	31.3962	16.85	14.76	13.09
174	2M03292155+3121104	52.3399	31.3529	12.39	11.72	11.37
175	2M03292187+3115363	52.3411	31.2601	11.18	10.15	9.50
176	2M03292204+3124153	52.3418	31.4043	12.00	11.27	11.00
177	2M03292293+3122355	52.3456	31.3765	17.07	16.07	15.59
178	2M03292314+3120303	52.3465	31.3417	12.40	11.65	11.23
179	2M03292322+3126531	52.3469	31.4481	13.59	12.70	12.24
180	2M03292349+3123309	52.3479	31.3919	12.84	11.76	11.36
181	2M03292369+3125095	52.3487	31.4193	14.04	12.94	12.37
182	2M03292407+3119577	52.3504	31.3327	15.52	14.24	13.57
183	2M03292445+3128149	52.3519	31.4708	14.04	13.17	12.69
184	2M03292483+3124062	52.3535	31.4017	14.43	13.77	13.38
185	2M03292591+3126401	52.3580	31.4445	11.00	9.99	9.51
186	2M03292681+3126475	52.3617	31.4465	10.83	9.99	9.68
187	2M03292798+3125109	52.3666	31.4197	17.66	16.36	14.95
188	2M03292815+3116285	52.3673	31.2746	13.05	12.50	12.09
189	2M03292925+3118347	52.3720	31.3096	12.59	11.37	10.96
190	2M03292978+3121027	52.3742	31.3507	12.65	11.62	11.16
191	2M03293038+3119034	52.3767	31.3176	12.11	11.39	11.03
192	2M03293053+3127280	52.3772	31.4578	13.81	13.01	12.60
193	2M03293255+3124370	52.3857	31.4102	13.66	12.43	11.61
194	2M03293261+3109479	52.3859	31.1633	17.14	16.14	15.28
195	2M03293286+3127126	52.3870	31.4535	13.35	12.60	12.28
196	2M03293387+3120362	52.3912	31.3434	16.56	15.68	15.48
197	2M03293430+3117433	52.3930	31.2954	12.03	11.31	11.06
198	2M03293476+3129081	52.3948	31.4856	13.65	12.20	11.53
199	2M03293773+3122024	52.4072	31.3674	13.99	13.39	12.96
200	2M03294415+3119478	52.4340	31.3298	17.39	16.28	15.29
201	2M03294640+3120394	52.4433	31.3443	12.36	11.74	11.47
202	2M03295048+3118305	52.4604	31.3085	14.36	13.80	13.53
203	2M03295403+3120529	52.4752	31.3480	11.94	11.14	10.59
204	2M03295721+3126214	52.4884	31.4393	12.37	11.51	11.20
205	2M03302246+3132403	52.5935	31.5446	16.24	15.84	14.88

NOTE. — Table 1 will be published electronically.

TABLE 2
Fit parameters for all observed APOGEE Spectra in NGC 1333

ObjID	MJD [days]	v_r [km s^{-1}]	σ	$v \sin i$ [km s^{-1}]	σ	$T_{\rm eff}$ [K]	σ	$\log g$ [log$_{10}$ cm s^{-2}]	σ	r_H	σ	red-χ^2	S/N
1	56671.05549	-29.24	0.95	90.48	1.38	6110.00	40.00	3.66	0.05	0.24	0.02	5.4	190
1	56674.05859	-25.11	0.87	99.16	1.50	5850.00	70.00	3.68	0.08	0.06	0.01	9.5	220
1	56563.49856	-29.28	1.20	90.96	1.78	6120.00	50.00	3.74	0.05	0.17	0.02	3.7	160
1	56607.32096	177.85	0.02	0.01	0.58	3890.00	30.00	4.15	0.09	0.00	0.00	551.5	180
1	56561.31439	-28.21	0.67	91.93	1.07	6120.00	30.00	3.70	0.03	0.21	0.01	9.3	280
1	56236.22732	-32.07	0.71	88.04	0.98	5980.00	20.00	3.60	0.02	0.22	0.01	28.4	270
1	56315.22693	-33.26	0.65	91.20	0.88	6150.00	40.00	3.85	0.05	0.18	0.01	35.5	320
2	56671.05549	9.91	0.22	3.01	2.26	3540.00	20.00	3.93	0.08	0.13	0.04	5.3	50
2	56674.05859	9.66	0.19	2.26	3.07	3630.00	30.00	4.21	0.08	0.08	0.03	3.8	50
2	56563.49856	10.02	0.35	6.45	1.79	3520.00	20.00	3.94	0.08	0.11	0.04	2.5	40
2	56607.32096	9.22	0.28	6.72	1.21	3520.00	20.00	3.91	0.08	0.17	0.04	2.8	40
2	56561.31439	10.27	0.24	7.27	1.02	3530.00	20.00	3.96	0.06	0.08	0.03	5.7	70
2	56236.22732	9.36	0.25	5.55	1.40	3540.00	20.00	3.97	0.07	0.10	0.03	5.6	70
2	56315.22693	9.62	0.29	5.60	1.59	3600.00	50.00	4.18	0.14	0.07	0.04	11.1	70
4	56671.05549	-2.33	15.95	72.26	27.27	6760.00	120.00	3.20	0.20	0.57	0.22	3.0	20
4	56674.05859	-6.83	9.75	89.94	16.80	6610.00	240.00	3.44	0.23	0.17	0.12	2.4	30
4	56563.49856	-1.19	16.71	88.50	26.94	6780.00	160.00	3.26	0.29	0.37	0.22	1.5	20
4	56607.32096	-8.29	9.72	91.31	13.73	6660.00	290.00	3.38	0.22	0.30	0.25	1.5	20
4	56561.31439	-7.71	5.33	79.91	7.94	6710.00	120.00	3.37	0.16	0.39	0.08	1.8	30
4	56236.22732	-9.27	5.92	75.00	8.51	6980.00	70.00	3.56	0.19	0.35	0.14	1.4	30
4	56315.22693	-14.07	4.99	84.65	7.28	6410.00	40.00	3.38	0.11	0.23	0.15	1.6	40
5	56561.31439	5.56	2.71	26.25	3.89	2780.00	80.00	2.99	0.28	0.01	0.05	4.1	10
5	56236.22732	5.86	2.88	34.78	5.25	2800.00	80.00	3.23	0.33	0.03	0.15	1.7	10
5	56315.22693	1.28	6.18	28.98	9.09	2800.00	160.00	4.22	0.83	0.01	0.06	7.9	10
8	56561.31439	34.78	1.88	8.80	8.41	5550.00	450.00	5.49	0.09	0.20	0.25	5.1	10
8	56236.22732	34.59	1.25	9.32	4.43	5890.00	220.00	5.49	0.04	0.01	0.05	3.4	20
8	56315.22693	35.44	1.21	6.32	6.91	5750.00	310.00	5.49	0.07	0.07	0.16	3.0	10
10	56671.05549	9.57	0.88	28.70	1.42	3320.00	20.00	3.90	0.12	0.15	0.05	3.1	40
10	56674.05859	9.19	0.76	28.61	1.29	3320.00	20.00	3.97	0.11	0.16	0.05	2.1	40
10	56563.49856	9.64	1.00	26.57	1.79	3320.00	20.00	3.80	0.15	0.19	0.07	1.6	30
10	56607.32096	8.71	0.76	27.26	1.25	3330.00	20.00	3.83	0.10	0.20	0.05	1.9	40
10	56561.31439	10.28	0.81	27.09	1.44	3310.00	20.00	3.83	0.12	0.21	0.06	2.8	40
10	56236.22732	9.28	0.56	27.63	0.95	3330.00	10.00	3.95	0.07	0.17	0.03	2.5	50
10	56315.22693	9.36	0.54	28.10	0.89	3320.00	10.00	3.91	0.08	0.17	0.03	2.8	50
11	56671.05549	8.21	0.64	54.26	0.93	3730.00	20.00	3.50	0.04	0.11	0.02	4.6	80
11	56674.05859	8.08	0.51	55.13	0.85	3850.00	20.00	3.79	0.05	0.09	0.01	4.0	80
11	56563.49856	7.90	0.69	52.78	0.96	3840.00	40.00	3.77	0.09	0.17	0.03	2.5	60
11	56607.32096	8.00	0.69	53.00	1.11	3730.00	20.00	3.67	0.04	0.14	0.02	4.5	80
11	56561.31439	7.89	0.86	51.61	1.38	3720.00	20.00	3.69	0.05	0.13	0.03	9.3	100
11	56236.22732	60.27	10.48	312.73	9.23	3400.00	40.00	2.54	0.16	0.00	0.00	82.7	100
11	56315.22693	9.60	0.54	53.65	0.87	3750.00	20.00	3.64	0.03	0.14	0.02	6.7	110
12	56671.05549	9.19	0.22	11.02	0.68	3850.00	20.00	4.18	0.05	0.14	0.02	6.9	80
12	56674.05859	9.45	0.16	11.12	0.50	3890.00	10.00	4.16	0.03	0.11	0.02	6.7	90
12	56563.49856	8.53	0.31	12.83	0.93	3990.00	20.00	4.41	0.07	0.19	0.03	3.6	60
12	56607.32096	9.29	0.28	12.26	0.80	3860.00	20.00	4.19	0.04	0.16	0.03	5.3	80
12	56561.31439	9.58	0.29	13.37	0.81	3870.00	20.00	4.22	0.05	0.13	0.02	8.4	90
12	56236.22732	9.22	0.23	12.75	0.68	3990.00	20.00	4.35	0.05	0.13	0.02	8.9	110
12	56315.22693	9.33	0.23	11.85	0.67	3910.00	20.00	4.18	0.04	0.09	0.02	9.0	90
13	56561.31439	148.19	0.05	0.02	0.08	450.00	0.00	3.00	0.01	2.58	0.09	13.4	0
13	56236.22732	11.15	37.12	71.47	57.06	3960.00	660.00	1.16	2.53	1.16	2.80	1.6	0
13	56315.22693	-1455.82	316.97	712.29	299.44	430.00	30.00	4.82	0.43	7.84	4.36	1.4	0
17	56236.22732	97.97	38.13	147.92	66.20	4780.00	580.00	4.89	0.96	0.03	0.24	1.8	10
17	56315.22693	-85.17	17.96	138.79	28.89	460.00	20.00	4.40	0.17	1.67	0.48	2.4	0
18	56671.05549	7.26	2.29	27.69	3.51	3250.00	180.00	3.55	0.62	0.22	0.21	3.0	20
18	56674.05859	8.68	1.55	21.90	2.98	3240.00	70.00	4.01	0.21	0.16	0.11	2.2	20
18	56563.49856	8.18	2.15	24.60	3.81	3250.00	70.00	3.99	0.29	0.21	0.15	1.3	10
18	56607.32096	9.25	1.62	23.34	2.69	3230.00	60.00	3.93	0.17	0.20	0.11	1.7	20
18	56561.31439	10.14	1.45	25.37	2.51	3290.00	40.00	3.82	0.19	0.18	0.10	2.6	20
18	56236.22732	9.53	1.25	21.02	2.31	3260.00	50.00	3.73	0.19	0.27	0.11	1.9	20
18	56315.22693	7.19	2.05	25.30	3.92	3050.00	90.00	2.67	0.22	1.15	0.31	2.9	20
19	56674.05859	10.28	1.03	60.34	1.73	4270.00	30.00	3.77	0.07	0.40	0.04	2.7	60
19	56563.49856	9.84	3.27	63.94	5.34	4240.00	100.00	3.59	0.20	1.24	0.19	1.5	30
19	56607.32096	9.12	0.99	56.24	1.45	4250.00	30.00	3.61	0.07	0.50	0.04	2.3	70
19	56561.31439	11.85	2.80	59.70	4.67	4090.00	70.00	3.52	0.16	1.23	0.15	5.5	60
20	56671.05549	6.82	0.46	24.65	0.65	3030.00	20.00	2.81	0.05	0.29	0.05	5.0	70
22	56671.05549	7.81	1.31	17.61	2.66	2790.00	140.00	3.39	1.11	0.12	0.27	3.4	20
22	56674.05859	7.50	0.93	17.19	2.01	2750.00	80.00	3.72	0.51	0.05	0.07	1.8	20
22	56563.49856	7.98	1.24	17.70	2.35	2700.00	80.00	3.29	0.50	0.12	0.12	1.5	10
22	56607.32096	6.17	1.82	20.07	4.32	2710.00	90.00	4.50	0.43	0.15	0.17	2.7	20
22	56561.31439	7.98	1.20	18.21	2.36	2760.00	80.00	3.22	0.34	0.12	0.14	3.6	20
22	56236.22732	8.42	0.92	17.12	1.80	2710.00	60.00	4.06	0.34	0.24	0.10	2.0	20
22	56315.22693	7.31	0.91	18.20	1.79	2700.00	40.00	3.51	0.26	0.04	0.06	2.3	20
23	56236.22732	7.77	0.34	26.70	0.52	3440.00	20.00	3.27	0.05	0.19	0.02	12.7	130

Foster, J.B. et al.

TABLE 2 — *Continued*

ObjID	MJD [days]	v_r [km s^{-1}]	σ	$v \sin i$ [km s^{-1}]	σ	T_{eff} [K]	σ	$\log g$ [log$_{10}$ cm s^{-2}]	σ	r_H	σ	red-χ^2	S/N
24	56561.31439	-31.40	2.28	5.75	10.77	6230.00	600.00	5.09	0.96	0.13	0.32	1.8	10
24	56236.22732	-13.50	179.49	622.12	242.44	3630.00	450.00	2.57	0.65	0.03	0.33	1.6	10
24	56315.22693	11.74	69.29	125.35	187.59	5660.00	1150.00	5.42	0.42	0.01	0.09	2.2	0
25	56561.31439	-20.95	6.07	17.73	12.49	2980.00	380.00	3.69	1.88	0.90	1.23	4.6	10
25	56236.22732	-20.91	3.21	16.07	8.70	3040.00	120.00	4.65	0.85	0.41	0.32	2.8	10
25	56315.22693	154.79	145.68	131.68	216.63	5130.00	1640.00	5.10	2.09	1.01	1.33	2.1	10
28	56671.05549	6.77	1.32	23.28	2.54	3320.00	40.00	3.63	0.22	0.23	0.11	4.2	30
28	56563.49856	7.11	1.06	22.41	1.88	3310.00	30.00	3.67	0.16	0.27	0.10	1.4	20
28	56607.32096	6.71	0.91	21.00	1.66	3360.00	30.00	3.69	0.15	0.38	0.09	1.7	30
28	56561.31439	6.07	1.09	21.32	1.97	3360.00	40.00	3.70	0.17	0.39	0.11	3.4	30
28	56236.22732	5.06	0.95	18.58	2.14	3350.00	30.00	3.73	0.17	0.91	0.15	1.8	30
29	56315.22693	8.30	0.36	17.62	0.70	2880.00	20.00	3.77	0.14	0.02	0.03	4.1	60
33	56674.05859	8.98	0.92	34.07	1.65	3680.00	30.00	3.98	0.11	0.11	0.04	2.1	30
33	56315.22693	13.31	0.96	34.78	1.65	3650.00	40.00	3.75	0.09	0.20	0.04	2.8	40
34	56674.05859	17.89	1.02	41.28	1.95	3190.00	20.00	3.07	0.07	2.92	0.17	3.0	130
34	56236.22732	6.89	0.22	15.70	0.41	3160.00	10.00	3.13	0.03	0.63	0.04	9.8	130
34	56315.22693	5.91	0.11	18.64	0.17	3180.00	0.00	3.14	0.02	0.62	0.02	12.0	170
35	56671.05549	7.80	1.14	24.99	2.08	3090.00	40.00	3.68	0.22	0.15	0.09	2.9	30
37	56671.05549	8.80	0.29	15.31	0.86	4290.00	20.00	4.26	0.06	0.29	0.02	9.5	100
37	56674.05859	8.35	0.21	15.58	0.53	4240.00	10.00	4.28	0.04	0.34	0.02	6.9	100
37	56563.49856	7.97	0.31	16.30	0.76	4420.00	30.00	4.47	0.07	0.30	0.02	4.2	70
37	56607.32096	8.66	0.26	15.86	0.72	4370.00	20.00	4.38	0.06	0.35	0.02	5.4	90
37	56561.31439	8.24	0.27	16.61	0.58	4350.00	20.00	4.35	0.06	0.28	0.02	6.6	90
37	56236.22732	8.15	0.23	15.73	0.60	4400.00	30.00	4.39	0.06	0.28	0.02	8.5	110
37	56315.22693	8.42	0.21	15.74	0.48	4260.00	10.00	4.23	0.04	0.26	0.01	10.5	130
39	56561.31439	7.80	1.06	26.03	1.69	2600.00	40.00	3.05	0.22	0.00	0.02	5.5	40
40	56671.05549	8.13	0.30	12.53	0.80	3670.00	20.00	4.07	0.08	0.24	0.03	5.4	70
40	56563.49856	8.20	0.42	13.80	1.16	3700.00	20.00	4.02	0.08	0.22	0.04	3.2	50
40	56607.32096	6.72	0.36	14.10	0.89	3530.00	20.00	3.76	0.05	0.25	0.04	3.5	60
40	56561.31439	8.23	0.29	12.79	0.73	3690.00	20.00	4.02	0.07	0.21	0.03	5.7	80
40	56236.22732	6.96	0.26	12.86	0.71	3540.00	20.00	3.75	0.05	0.24	0.03	5.8	80
41	56563.49856	8.21	1.59	23.04	2.76	2990.00	50.00	3.76	0.35	0.11	0.10	1.6	20
41	56607.32096	6.72	1.37	25.02	2.59	2940.00	40.00	3.92	0.25	0.08	0.08	1.9	20
42	56671.05549	10.09	0.64	15.63	1.63	3730.00	40.00	3.81	0.12	0.24	0.06	2.9	30
42	56563.49856	9.12	0.94	16.00	2.32	3900.00	80.00	4.15	0.16	0.34	0.08	1.4	20
42	56607.32096	9.24	2.09	15.24	5.53	4030.00	190.00	4.31	0.45	0.72	0.25	1.2	10
42	56561.31439	9.56	0.70	15.62	1.59	3760.00	70.00	3.84	0.13	0.36	0.06	2.6	30
43	56236.22732	7.50	0.58	15.52	1.03	3050.00	20.00	3.75	0.19	0.07	0.05	2.9	40
44	56315.22693	8.92	0.23	10.74	0.68	3750.00	20.00	3.83	0.05	0.62	0.04	5.9	80
48	56674.05859	8.13	0.38	14.09	0.91	3690.00	20.00	3.82	0.08	0.23	0.04	2.8	40
50	56674.05859	8.43	0.71	18.12	1.45	2780.00	80.00	3.43	0.56	0.01	0.07	2.3	30
51	56674.05859	8.16	0.59	9.79	1.84	3500.00	40.00	3.83	0.14	0.20	0.08	1.8	20
52	56236.22732	8.36	0.32	17.62	0.79	4130.00	30.00	4.27	0.06	0.89	0.03	3.8	80
56	56671.05549	9.08	0.30	7.94	1.26	3900.00	30.00	4.05	0.08	0.35	0.04	3.2	40
58	56315.22693	-309.02	41.27	463.52	77.24	3010.00	400.00	-0.27	0.75	0.33	0.37	1.4	0
59	56671.05549	8.69	0.39	33.21	0.56	5610.00	30.00	4.38	0.05	0.15	0.02	58.3	340
59	56563.49856	8.21	0.16	33.07	0.23	5660.00	10.00	4.33	0.02	0.08	0.01	13.6	250
59	56607.32096	8.39	0.13	33.47	0.21	5680.00	10.00	4.35	0.02	0.08	0.01	19.3	310
59	56561.31439	8.71	0.09	33.31	0.14	5680.00	10.00	4.28	0.01	0.06	0.00	39.7	420
59	56236.22732	7.44	0.10	32.42	0.17	5660.00	10.00	4.39	0.02	0.05	0.01	37.0	370
60	56671.05549	7.40	0.30	17.89	0.70	3460.00	20.00	3.86	0.06	0.10	0.03	4.9	70
61	56236.22732	7.38	0.40	10.11	1.11	3310.00	10.00	3.96	0.09	0.32	0.05	3.5	60
62	56315.22693	6.13	0.86	22.20	1.23	3920.00	30.00	3.96	0.07	0.00	0.00	14.2	70
63	56671.05549	10.50	0.53	16.14	1.33	4120.00	30.00	4.19	0.11	0.15	0.04	3.0	30
63	56674.05859	9.30	0.53	16.18	1.21	4140.00	40.00	4.24	0.10	0.08	0.04	3.2	30
63	56563.49856	9.52	0.56	17.98	1.42	4210.00	50.00	4.32	0.11	0.14	0.04	1.8	30
63	56607.32096	9.29	0.55	17.50	1.31	4200.00	50.00	4.29	0.11	0.12	0.03	3.5	40
63	56561.31439	9.73	0.47	16.02	1.09	4240.00	40.00	4.33	0.09	0.12	0.03	3.9	40
63	56236.22732	10.08	0.35	16.08	0.93	4260.00	30.00	4.24	0.07	0.11	0.02	3.4	50
63	56315.22693	9.98	0.46	16.01	1.13	4100.00	30.00	4.21	0.09	0.23	0.04	4.7	50
65	56563.49856	8.89	1.84	20.47	3.22	2760.00	130.00	2.94	0.33	0.01	0.06	3.6	10
65	56607.32096	9.73	1.09	21.09	1.86	2650.00	40.00	3.71	0.44	0.00	0.02	1.5	20
66	56315.22693	98.00	28.27	78.82	32.89	3660.00	460.00	3.58	0.95	2.20	1.65	2.2	10
71	56236.22732	8.69	0.70	20.01	1.61	4540.00	100.00	4.32	0.15	0.26	0.06	2.0	30
74	56561.31439	4.98	3.28	23.09	9.04	3820.00	110.00	5.35	0.33	3.07	0.50	7.8	80
76	56674.05859	8.24	0.54	22.11	1.22	4010.00	20.00	4.30	0.08	0.09	0.03	2.6	40
76	56315.22693	8.92	0.36	21.14	0.80	4020.00	20.00	4.25	0.06	0.14	0.02	3.1	50
77	56315.22693	7.34	1.01	42.77	1.57	3120.00	10.00	3.49	0.09	0.11	0.05	2.3	40
78	56671.05549	10.91	1.53	16.31	3.37	3560.00	110.00	3.52	0.26	0.19	0.13	5.3	10
79	56674.05859	-57.12	14.87	77.95	21.92	400.00	0.00	4.43	0.05	1.79	0.37	5.4	0
79	56563.49856	-192.92	37.34	16.41	32.20	1260.00	2060.00	3.21	1.44	0.92	21.75	1.5	0
79	56607.32096	-706.59	249.18	210.86	627.91	1450.00	5130.00	4.47	4.29	0.29	3.11	2.0	0
81	56561.31439	-226.61	1542.90	587.08	1292.89	2660.00	950.00	2.01	4.50	0.17	12.00	2.5	10
86	56563.49856	-1.02	0.58	10.75	1.92	3760.00	40.00	4.59	0.13	0.12	0.05	1.5	30

TABLE 2 — *Continued*

ObjID	MJD [days]	v_r [km s^{-1}]	σ	$v \sin i$ [km s^{-1}]	σ	$T_{\rm eff}$ [K]	σ	$\log g$ [log$_{10}$ cm s^{-2}]	σ	r_H	σ	red-χ^2	S/N
86	56607.32096	-1.23	0.58	12.49	1.68	3910.00	100.00	4.83	0.22	0.22	0.06	2.0	40
86	56315.22693	-1.16	0.51	7.94	2.01	3760.00	40.00	4.83	0.19	0.13	0.06	5.9	50
87	56674.05859	7.93	1.06	16.81	2.63	3710.00	50.00	4.13	0.19	1.23	0.18	1.8	30
87	56236.22732	8.36	1.11	20.17	2.76	3490.00	40.00	3.75	0.14	1.36	0.18	1.8	40
91	56561.31439	12.29	3.55	18.03	6.84	2680.00	230.00	4.64	1.69	0.58	0.61	1.9	10
91	56236.22732	26.09	282.26	611.58	281.62	4680.00	310.00	2.02	0.17	0.01	0.05	2.6	10
91	56315.22693	-226.39	74.70	466.39	95.84	2550.00	190.00	1.24	0.86	0.96	1.38	2.4	10
93	56674.05859	297.16	79.37	560.41	89.59	3940.00	260.00	3.76	0.45	0.13	0.31	1.9	10
93	56561.31439	-165.19	27.44	239.24	32.61	5730.00	350.00	5.49	0.08	0.11	0.26	3.1	20
94	56563.49856	8.15	0.90	32.51	1.64	4610.00	80.00	4.30	0.12	0.56	0.06	8.2	90
94	56607.32096	9.24	0.71	33.49	1.41	4770.00	120.00	4.58	0.15	0.58	0.05	9.7	110
94	56315.22693	11.75	1.59	34.31	3.62	4510.00	110.00	4.37	0.21	0.76	0.12	49.9	150
96	56671.05549	8.75	2.45	41.99	3.91	2960.00	40.00	3.69	0.26	0.01	0.05	2.9	20
97	56671.05549	10.72	0.83	33.99	1.44	3700.00	30.00	3.67	0.08	0.25	0.04	3.4	50
97	56674.05859	9.65	0.59	33.27	1.01	3710.00	20.00	3.72	0.05	0.29	0.03	2.0	50
97	56563.49856	9.79	0.95	34.37	1.75	3730.00	80.00	3.72	0.13	0.33	0.05	1.6	30
97	56607.32096	9.93	0.80	35.54	1.41	3730.00	40.00	3.70	0.07	0.30	0.04	1.8	40
97	56561.31439	10.62	0.71	34.01	1.51	3740.00	40.00	3.74	0.08	0.28	0.04	2.8	50
97	56236.22732	6.74	0.69	34.26	1.23	3760.00	250.00	3.76	0.36	0.31	0.10	3.0	60
97	56315.22693	7.09	0.97	34.55	1.65	3710.00	30.00	3.72	0.07	0.31	0.05	4.5	50
105	56236.22732	-47.24	366.32	483.26	606.64	4470.00	940.00	2.14	0.95	0.06	1.64	1.8	0
110	56236.22732	5.48	1.96	70.13	3.22	4010.00	50.00	3.33	0.09	0.45	0.07	3.6	50
111	56561.31439	3.17	3.93	1.57	11.00	4090.00	440.00	4.03	0.87	1.84	1.13	2.8	10
111	56236.22732	-33.43	17.62	138.57	29.03	400.00	10.00	4.55	0.11	6.32	2.15	9.6	10
111	56315.22693	-434.51	31.91	231.82	36.57	3360.00	290.00	-0.41	0.52	1.57	0.66	1.5	0
116	56315.22693	9.28	0.61	30.23	1.04	3930.00	20.00	4.00	0.06	0.25	0.03	5.0	70
118	56671.05549	9.60	1.29	21.21	2.46	3150.00	40.00	3.57	0.29	0.12	0.12	2.7	20
118	56674.05859	8.67	1.31	16.03	2.89	3230.00	60.00	4.20	0.29	0.32	0.13	3.0	20
118	56563.49856	9.98	1.66	21.26	3.57	3210.00	70.00	3.92	0.23	0.23	0.11	1.4	20
118	56607.32096	8.66	1.24	19.15	2.42	3210.00	70.00	3.85	0.29	0.25	0.09	1.4	20
118	56561.31439	9.66	1.08	22.00	2.17	3170.00	40.00	3.89	0.21	0.20	0.07	2.3	30
118	56315.22693	9.61	1.14	19.66	2.02	3120.00	30.00	3.61	0.24	0.18	0.11	2.1	20
122	56671.05549	10.34	6.34	37.45	8.95	3430.00	170.00	3.46	0.56	0.93	0.51	3.3	10
125	56236.22732	-244.15	95.44	249.68	101.23	4500.00	370.00	2.03	0.40	0.02	0.22	3.9	10
127	56671.05549	-189.27	0.33	0.02	0.23	4310.00	10.00	4.32	0.09	0.00	0.00	76.6	0
127	56674.05859	-6.54	33.34	36.62	64.40	1790.00	620.00	4.76	1.06	0.04	0.29	1.8	0
127	56563.49856	104.92	1.13	74.95	0.75	780.00	30.00	3.00	0.20	0.00	0.11	13520.0	0
127	56607.32096	-168.35	0.09	0.01	0.19	790.00	0.00	3.00	0.02	0.00	0.01	175.9	0
127	56561.31439	-164.15	0.07	0.02	0.22	430.00	0.00	3.84	0.02	0.77	0.07	70.6	0
127	56236.22732	31.25	0.79	16.53	0.74	6600.00	50.00	2.67	0.20	0.05	0.05	0.1	0
127	56315.22693	-166.08	2930.73	4188.49	3029.96	430.00	40.00	3.83	0.53	0.56	1.22	1.4	0
128	56236.22732	9.57	6.44	529.40	15.76	7000.00	0.00	3.85	0.04	0.18	0.03	3.2	150
130	56563.49856	7.24	0.57	69.18	0.76	5660.00	30.00	3.77	0.05	0.28	0.02	5.1	230
130	56607.32096	9.64	0.50	69.67	0.91	5670.00	20.00	3.84	0.03	0.30	0.02	13.3	280
130	56561.31439	5.20	0.34	69.10	0.58	5530.00	10.00	3.69	0.02	0.32	0.01	15.3	350
131	56561.31439	9.47	1.85	15.71	3.73	3120.00	50.00	3.62	0.41	0.32	0.21	2.3	10
133	56671.05549	33.04	16.32	236.84	22.17	6000.00	230.00	3.98	0.30	0.20	0.11	1.5	40
133	56674.05859	27.61	22.42	275.09	22.12	5650.00	930.00	3.83	1.15	0.39	0.24	1.8	50
133	56563.49856	16.70	32.61	183.31	53.24	6050.00	410.00	4.03	0.48	0.34	0.23	1.3	30
133	56607.32096	10.56	19.13	212.86	32.42	5250.00	240.00	3.19	0.38	0.48	0.22	1.2	30
133	56561.31439	62.92	25.38	331.32	69.38	5330.00	170.00	3.25	0.27	0.05	0.10	2.7	50
133	56236.22732	20.48	11.23	216.30	15.90	5770.00	130.00	3.81	0.18	0.16	0.08	1.6	50
133	56315.22693	51.70	14.20	311.76	19.42	6190.00	80.00	4.38	0.13	0.14	0.09	2.0	50
136	56671.05549	6.43	1.12	6.81	4.40	2630.00	100.00	4.76	0.41	0.23	0.20	7.4	20
136	56674.05859	6.24	0.77	11.34	1.86	2550.00	70.00	3.13	0.32	0.08	0.10	2.2	10
136	56563.49856	5.93	0.86	11.97	2.49	2510.00	100.00	4.43	0.46	0.27	0.24	1.9	10
136	56607.32096	7.07	0.95	8.86	3.39	2000.00	40.00	4.99	0.16	0.34	0.19	4.4	20
137	56674.05859	7.85	1.18	20.54	2.04	2620.00	50.00	3.82	0.50	0.00	0.02	2.1	20
138	56236.22732	8.33	1.48	21.13	2.53	3100.00	40.00	3.69	0.29	0.23	0.13	1.7	20
140	56315.22693	25.41	75.87	2.09	184.63	1900.00	1030.00	5.25	4.16	3.34	9.86	2.7	0
145	56563.49856	6.72	1.22	21.71	1.86	3010.00	40.00	4.03	0.25	0.04	0.07	1.9	20
145	56607.32096	6.60	1.54	23.96	2.15	2980.00	40.00	3.91	0.23	0.01	0.04	3.5	30
145	56315.22693	6.15	0.67	22.81	1.06	2950.00	20.00	3.73	0.22	0.00	0.02	2.2	40
152	56561.31439	9.36	4.46	32.09	7.02	2660.00	150.00	3.74	1.42	0.01	0.10	2.3	10
152	56236.22732	8.00	4.16	32.86	7.38	2750.00	120.00	3.27	0.74	0.22	0.27	1.8	10
152	56315.22693	9.08	2.68	19.40	4.79	2540.00	70.00	2.00	0.39	0.70	0.72	2.3	10
158	56674.05859	7.79	1.24	24.72	2.02	3380.00	120.00	3.92	0.27	0.14	0.09	1.5	20
158	56315.22693	8.07	1.16	25.45	1.79	3330.00	40.00	3.42	0.14	0.32	0.10	1.8	20
159	56671.05549	9.00	0.64	22.70	1.41	3480.00	20.00	4.03	0.11	0.19	0.05	2.8	40
159	56674.05859	8.17	0.43	19.71	0.96	3510.00	20.00	4.11	0.08	0.20	0.03	2.3	50
159	56561.31439	8.59	0.57	20.50	1.16	3470.00	20.00	4.01	0.09	0.20	0.04	2.2	40
160	56671.05549	6.59	0.24	19.90	0.56	3320.00	10.00	3.80	0.05	0.19	0.02	4.2	80
160	56674.05859	6.11	0.36	19.37	0.81	3310.00	10.00	3.80	0.07	0.16	0.03	5.7	70
160	56563.49856	7.01	0.39	23.93	0.68	3300.00	10.00	3.79	0.06	0.14	0.03	2.7	60

TABLE 2 — *Continued*

ObjID	MJD [days]	v_r [km s^{-1}]	σ	$v \sin i$ [km s^{-1}]	σ	T_{eff} [K]	σ	$\log g$ [$\log_{10}$ cm s^{-2}]	σ	r_H	σ	red-χ^2	S/N
160	56607.32096	6.24	0.33	22.66	0.59	3310.00	10.00	3.79	0.05	0.17	0.02	3.4	70
160	56561.31439	6.99	0.31	24.00	0.54	3300.00	10.00	3.78	0.05	0.15	0.02	5.4	90
160	56236.22732	6.88	0.20	17.29	0.42	3310.00	10.00	3.73	0.04	0.19	0.02	6.6	110
160	56315.22693	7.38	0.20	18.17	0.33	3310.00	10.00	3.84	0.04	0.19	0.02	7.3	110
162	56563.49856	6.75	0.35	20.22	0.70	3900.00	20.00	3.81	0.05	0.53	0.03	16.2	150
162	56607.32096	5.91	0.29	19.65	0.50	3890.00	10.00	3.81	0.04	0.58	0.02	19.9	180
162	56236.22732	6.60	0.27	19.84	0.67	3910.00	10.00	3.81	0.04	0.55	0.02	38.4	250
163	56561.31439	27.13	37.35	62.82	45.64	4070.00	760.00	3.44	1.86	0.03	0.17	2.1	0
163	56236.22732	389.84	165.53	848.74	216.30	510.00	120.00	3.07	0.38	0.71	0.62	1.6	0
163	56315.22693	-83.25	1.10	0.11	2.54	430.00	0.00	4.06	0.04	1.25	0.11	6.8	0
167	56315.22693	8.07	0.17	13.49	0.42	3900.00	10.00	4.07	0.03	0.33	0.02	7.9	110
168	56674.05859	21.25	6.09	435.73	13.77	7000.00	10.00	3.91	0.03	0.83	0.05	6.1	270
168	56561.31439	1.59	5.03	495.94	12.40	7000.00	0.00	3.99	0.03	0.81	0.05	8.2	270
168	56236.22732	47.09	4.41	493.29	11.77	7000.00	0.00	4.04	0.03	0.60	0.03	7.5	320
171	56671.05549	12.45	4.45	30.02	9.50	5640.00	760.00	5.48	0.31	1.07	0.75	4.1	20
171	56674.05859	8.07	1.95	36.73	3.83	4480.00	120.00	4.02	0.26	0.57	0.13	2.1	20
171	56563.49856	7.85	2.55	36.01	4.49	4480.00	170.00	4.49	0.27	1.30	0.20	1.5	20
171	56607.32096	11.33	1.76	33.12	3.67	4700.00	250.00	4.70	0.35	0.68	0.13	1.5	20
171	56561.31439	6.51	1.33	32.07	2.58	4970.00	160.00	4.97	0.19	0.99	0.11	1.9	40
171	56236.22732	5.06	1.69	35.72	3.47	4940.00	270.00	4.58	0.29	0.97	0.17	1.6	30
171	56315.22693	10.24	1.44	31.83	3.25	4720.00	330.00	4.69	0.44	1.03	0.14	2.4	40
173	56236.22732	10.31	6.16	31.65	9.85	2960.00	150.00	4.00	1.04	0.23	0.35	1.7	10
174	56671.05549	7.19	0.36	17.65	0.75	3080.00	10.00	3.54	0.08	0.07	0.04	3.3	50
174	56563.49856	7.98	0.59	18.86	1.01	3070.00	20.00	3.59	0.11	0.01	0.04	2.1	30
174	56607.32096	7.88	0.47	17.67	0.84	3060.00	20.00	3.68	0.11	0.05	0.04	2.2	40
174	56561.31439	7.30	3.29	18.44	6.04	2880.00	130.00	2.93	0.63	0.28	0.49	2.2	10
174	56236.22732	10.26	0.71	18.84	1.21	3120.00	10.00	3.37	0.10	0.02	0.05	11.4	70
175	56671.05549	16.88	1.56	46.34	3.28	4170.00	60.00	4.35	0.13	2.12	0.14	2.5	70
175	56674.05859	7.02	0.55	49.42	1.04	4210.00	10.00	4.36	0.05	0.79	0.03	4.8	110
175	56563.49856	14.12	2.22	46.17	3.89	4220.00	90.00	4.57	0.21	2.96	0.28	2.4	60
175	56607.32096	2.59	0.90	41.60	1.76	4210.00	30.00	4.50	0.08	1.79	0.08	2.9	90
175	56561.31439	11.78	1.75	45.52	3.02	3980.00	40.00	4.26	0.13	4.13	0.27	3.8	100
175	56236.22732	8.58	0.34	43.36	0.59	4240.00	10.00	4.50	0.03	0.76	0.02	12.0	160
175	56315.22693	3.13	1.06	45.40	2.15	4230.00	30.00	4.36	0.08	2.24	0.10	2.9	100
176	56671.05549	1.22	3.27	121.79	4.23	3330.00	30.00	4.06	0.14	0.18	0.05	4.0	70
178	56674.05859	6.38	0.23	12.32	0.59	3130.00	10.00	3.56	0.07	0.31	0.04	3.0	60
178	56315.22693	6.88	0.27	12.34	0.63	3120.00	10.00	3.48	0.05	0.37	0.04	3.6	60
179	56671.05549	6.73	0.59	14.83	1.46	3110.00	20.00	3.67	0.19	0.27	0.09	1.9	30
179	56674.05859	6.80	0.45	14.59	1.01	3120.00	20.00	3.76	0.14	0.21	0.06	2.1	30
180	56674.05859	5.53	0.49	17.01	1.19	3690.00	20.00	3.88	0.08	0.00	0.00	8.0	50
180	56563.49856	8.18	0.72	14.54	1.92	3720.00	50.00	4.04	0.13	0.17	0.07	4.2	30
180	56607.32096	7.54	0.43	13.50	1.10	3700.00	20.00	4.03	0.08	0.10	0.04	3.3	40
180	56561.31439	8.51	0.36	14.25	0.85	3680.00	20.00	4.00	0.08	0.11	0.03	3.4	50
181	56563.49856	7.70	1.93	28.83	3.03	3300.00	40.00	3.77	0.23	0.09	0.11	2.1	20
181	56607.32096	8.02	1.16	27.25	1.80	3250.00	30.00	3.91	0.12	0.10	0.06	1.5	20
181	56315.22693	9.81	1.00	26.18	1.52	3220.00	40.00	3.94	0.10	0.17	0.07	2.2	30
182	56561.31439	13.99	5.42	46.63	8.05	4090.00	170.00	2.86	0.42	0.01	0.08	3.1	10
182	56236.22732	8.08	3.86	39.31	5.78	3860.00	170.00	3.16	0.29	0.56	0.20	1.7	10
183	56671.05549	-106.39	0.23	7.15	1.82	3240.00	10.00	-0.50	0.00	0.00	0.00	12.8	0
183	56674.05859	-35.15	2.52	0.17	18.57	750.00	90.00	3.00	0.05	0.14	1.15	25857.3	0
183	56563.49856	1.43	0.11	39.97	0.10	490.00	0.00	3.80	0.04	0.00	0.00	22104.9	0
183	56607.32096	-131.69	2.13	0.01	3.12	790.00	70.00	3.00	0.61	0.00	0.40	135005.8	0
183	56561.31439	-10.38	4.20	57.47	2.15	400.00	0.00	5.00	0.01	0.00	0.00	0.3	0
183	56236.22732	-137.24	0.04	0.03	0.32	4110.00	20.00	3.99	0.09	0.00	0.00	1521.5	0
183	56315.22693	-170.81	0.15	0.02	0.25	1900.00	20.00	3.43	0.07	0.00	0.00	69.5	0
185	56561.31439	8.87	0.46	31.56	1.13	5260.00	70.00	4.84	0.08	0.51	0.05	3.6	90
185	56236.22732	8.72	1.04	50.59	1.81	5240.00	90.00	4.76	0.11	0.63	0.07	2.3	80
186	56563.49856	7.23	0.35	14.55	0.86	4030.00	20.00	4.24	0.07	0.25	0.03	7.3	80
186	56607.32096	7.27	0.28	15.13	0.61	3910.00	20.00	4.08	0.04	0.21	0.02	9.7	110
186	56315.22693	8.07	0.25	14.60	0.78	3940.00	20.00	4.09	0.05	0.21	0.02	19.3	150
188	56671.05549	7.15	0.90	28.05	1.49	2660.00	30.00	2.80	0.05	0.00	0.01	2.5	30
188	56674.05859	7.27	0.76	27.89	1.20	2620.00	20.00	2.90	0.07	0.00	0.01	2.0	30
188	56563.49856	6.52	1.05	27.25	1.58	2610.00	30.00	3.93	0.20	0.00	0.01	1.5	20
188	56607.32096	7.21	0.77	27.63	1.15	2600.00	20.00	3.96	0.13	0.00	0.01	1.8	30
188	56561.31439	6.45	0.61	28.20	1.07	2640.00	20.00	2.76	0.05	0.00	0.01	2.6	40
188	56236.22732	7.28	0.62	28.04	1.00	2620.00	20.00	3.92	0.13	0.00	0.00	2.5	40
188	56315.22693	7.75	0.60	28.22	1.02	2550.00	20.00	2.44	0.15	0.00	0.01	3.2	40
189	56671.05549	6.95	0.21	8.65	0.86	4100.00	20.00	4.25	0.06	0.11	0.02	4.4	60
189	56563.49856	6.76	0.30	9.81	1.07	4210.00	30.00	4.37	0.08	0.10	0.03	2.8	40
189	56607.32096	6.65	0.25	9.01	0.95	4180.00	40.00	4.37	0.07	0.09	0.02	3.9	60
189	56561.31439	7.17	0.27	9.87	0.99	4140.00	40.00	4.29	0.08	0.09	0.03	7.4	70
189	56236.22732	6.74	0.23	10.27	0.81	4220.00	30.00	4.34	0.06	0.13	0.02	5.7	70
190	56671.05549	8.68	0.31	14.39	0.67	3320.00	10.00	3.83	0.07	0.17	0.04	3.0	50
190	56674.05859	8.40	0.25	14.15	0.60	3310.00	10.00	3.85	0.06	0.20	0.03	2.6	50

TABLE 2 — *Continued*

ObjID	MJD [days]	v_r [km s^{-1}]	σ	$v \sin i$ [km s^{-1}]	σ	T_{eff} [K]	σ	$\log g$ [log$_{10}$ cm s^{-2}]	σ	r_H	σ	red-χ^2	S/N
190	56563.49856	14.08	0.86	23.15	1.82	3360.00	30.00	3.39	0.10	0.13	0.08	4.1	40
190	56607.32096	8.33	0.39	14.12	0.82	3300.00	10.00	3.85	0.08	0.17	0.04	2.3	50
190	56561.31439	9.48	0.42	15.23	0.88	3300.00	10.00	3.80	0.09	0.10	0.04	5.7	60
190	56236.22732	8.40	0.31	14.76	0.71	3320.00	10.00	3.74	0.06	0.21	0.03	3.2	60
190	56315.22693	8.25	0.25	14.20	0.58	3310.00	10.00	3.81	0.06	0.21	0.03	3.4	60
191	56674.05859	7.09	0.20	9.36	0.65	3310.00	10.00	3.67	0.07	0.24	0.03	3.1	50
191	56315.22693	6.94	0.18	9.65	0.55	3310.00	10.00	3.59	0.05	0.28	0.03	5.1	80
192	56671.05549	8.54	0.81	16.03	1.79	2930.00	40.00	3.99	0.21	0.03	0.06	2.0	20
192	56674.05859	8.12	0.76	16.30	1.63	2930.00	30.00	4.11	0.19	0.03	0.06	1.9	20
193	56671.05549	4.51	0.77	20.63	1.48	3070.00	30.00	3.58	0.15	0.46	0.09	2.5	40
193	56674.05859	5.65	0.72	20.54	1.27	3090.00	20.00	3.72	0.15	0.51	0.08	2.8	40
193	56563.49856	6.52	1.26	22.63	2.18	3080.00	40.00	3.53	0.19	0.67	0.14	1.5	30
193	56607.32096	8.32	0.96	12.00	2.47	3290.00	40.00	3.65	0.17	0.57	0.14	3.0	30
193	56561.31439	5.67	0.66	20.75	1.08	3080.00	20.00	3.56	0.11	0.56	0.07	2.4	50
193	56236.22732	4.68	0.84	20.22	1.63	3100.00	20.00	3.78	0.19	0.71	0.10	1.5	40
193	56315.22693	6.11	0.47	18.87	0.81	3060.00	20.00	3.59	0.09	0.44	0.06	2.2	40
195	56563.49856	9.59	1.00	17.00	2.12	3220.00	50.00	4.00	0.21	0.20	0.08	1.6	20
195	56607.32096	8.45	0.92	15.84	1.82	3190.00	40.00	4.10	0.19	0.21	0.08	1.9	30
195	56561.31439	9.21	0.68	16.84	1.30	3200.00	30.00	3.94	0.13	0.20	0.05	2.3	30
195	56236.22732	8.33	0.77	17.05	1.58	3180.00	30.00	3.91	0.16	0.25	0.06	2.0	30
195	56315.22693	8.33	0.83	16.34	1.79	3160.00	50.00	3.91	0.22	0.29	0.08	3.1	30
197	56671.05549	7.24	0.19	9.64	0.62	3470.00	10.00	3.99	0.06	0.14	0.03	4.2	70
197	56674.05859	7.24	0.18	9.51	0.60	3460.00	20.00	4.04	0.05	0.13	0.02	4.0	70
197	56563.49856	8.07	0.40	11.92	0.98	3370.00	20.00	3.82	0.09	0.07	0.04	2.8	50
197	56607.32096	7.04	0.30	9.77	0.86	3460.00	20.00	3.99	0.07	0.12	0.03	3.7	60
197	56561.31439	7.62	0.26	10.52	0.76	3460.00	20.00	4.03	0.05	0.11	0.03	4.3	70
197	56236.22732	7.05	0.23	9.74	0.73	3480.00	10.00	3.95	0.04	0.18	0.03	5.0	80
197	56315.22693	7.21	0.16	9.39	0.54	3480.00	10.00	3.98	0.05	0.15	0.02	5.9	80
198	56671.05549	17.36	0.54	7.02	2.53	6860.00	210.00	5.29	0.20	0.09	0.08	1.7	30
198	56674.05859	17.18	0.40	7.89	1.59	6660.00	60.00	5.01	0.09	0.14	0.04	1.8	40
198	56563.49856	16.90	0.56	7.90	2.27	6630.00	130.00	4.94	0.17	0.08	0.06	1.4	30
198	56607.32096	16.90	0.54	7.91	2.30	6620.00	150.00	5.13	0.19	0.14	0.07	2.3	40
198	56561.31439	16.98	0.41	7.46	1.57	6540.00	130.00	4.87	0.17	0.12	0.06	2.3	40
198	56236.22732	17.15	0.36	8.02	1.42	6680.00	80.00	5.11	0.12	0.11	0.04	1.9	40
198	56315.22693	16.86	0.39	7.03	1.71	6870.00	70.00	5.47	0.07	0.10	0.04	1.9	40
199	56671.05549	7.69	1.31	20.75	2.14	2690.00	60.00	3.45	0.48	0.01	0.04	2.1	20
199	56674.05859	7.09	1.05	20.98	1.96	2670.00	50.00	3.94	0.40	0.09	0.09	1.7	20
199	56563.49856	7.65	1.92	21.61	3.47	2660.00	100.00	3.55	0.74	0.04	0.14	1.7	10
199	56607.32096	7.78	1.18	22.19	2.01	2590.00	70.00	3.87	0.40	0.14	0.13	1.4	20
199	56561.31439	7.75	1.02	22.61	1.68	2610.00	60.00	3.14	0.37	0.00	0.03	2.0	20
199	56236.22732	7.63	0.93	20.32	1.66	2630.00	60.00	3.82	0.31	0.29	0.12	1.7	20
199	56315.22693	7.37	1.17	22.08	2.37	2560.00	60.00	4.00	0.32	0.29	0.13	2.8	20
201	56671.05549	6.97	0.67	32.24	1.11	3140.00	20.00	3.98	0.08	0.05	0.03	2.2	50
201	56674.05859	6.68	0.63	31.51	0.98	3130.00	10.00	4.00	0.07	0.07	0.03	2.6	50
201	56563.49856	6.29	1.03	31.35	1.56	3130.00	20.00	3.90	0.15	0.12	0.05	1.7	30
201	56607.32096	6.71	0.76	31.68	1.13	3130.00	20.00	3.98	0.10	0.10	0.04	2.0	50
201	56561.31439	15.24	1.07	30.19	2.13	3300.00	20.00	3.55	0.13	0.08	0.07	12.7	60
201	56236.22732	6.61	0.55	31.21	0.91	3120.00	10.00	3.96	0.08	0.11	0.03	2.4	60
201	56315.22693	7.06	0.49	30.50	0.87	3110.00	10.00	3.92	0.07	0.17	0.03	2.6	60
202	56561.31439	3.60	1.36	10.43	4.02	3360.00	70.00	4.58	0.33	0.20	0.13	2.0	20
202	56236.22732	2.99	1.16	9.78	4.00	3390.00	60.00	4.74	0.39	0.54	0.15	1.5	20
202	56315.22693	128.75	30.46	170.86	38.90	5380.00	870.00	5.47	0.28	0.99	1.01	3.0	10
203	56671.05549	7.22	0.33	13.10	0.75	3140.00	10.00	3.41	0.08	0.70	0.06	4.3	70
203	56674.05859	7.13	0.28	13.63	0.65	3140.00	10.00	3.42	0.06	0.85	0.06	3.9	70
203	56563.49856	7.97	0.48	15.21	1.03	3140.00	10.00	3.42	0.10	0.56	0.08	2.3	50
203	56607.32096	7.72	0.37	14.13	0.78	3130.00	10.00	3.45	0.06	0.77	0.06	3.1	70
203	56561.31439	7.78	0.29	14.86	0.58	3130.00	10.00	3.41	0.06	0.54	0.05	5.2	80
203	56236.22732	6.97	0.39	13.44	0.81	3140.00	10.00	3.41	0.07	0.84	0.07	5.8	90
203	56315.22693	6.95	0.28	12.76	0.61	3130.00	10.00	3.45	0.06	0.77	0.05	6.0	90
204	56671.05549	7.93	0.33	21.84	0.64	3580.00	30.00	3.81	0.06	0.10	0.03	2.9	50
204	56674.05859	7.88	0.27	21.44	0.52	3570.00	20.00	3.77	0.04	0.15	0.02	2.7	60
204	56563.49856	7.17	0.58	22.66	0.96	3650.00	30.00	3.84	0.08	0.17	0.04	2.2	40
204	56607.32096	7.43	0.38	21.31	0.63	3560.00	20.00	3.78	0.05	0.12	0.03	2.3	50
204	56561.31439	7.74	0.34	22.28	0.66	3560.00	20.00	3.73	0.05	0.12	0.03	4.0	70
204	56236.22732	7.29	0.50	21.59	0.96	3570.00	30.00	3.78	0.07	0.12	0.04	5.3	60
204	56315.22693	7.77	0.27	21.06	0.52	3620.00	30.00	3.78	0.05	0.18	0.02	3.8	70

NOTE. — Table 2 will be published electronically. Fit parameters are the effective temperature (T_{eff}), the veiling (r_H), the rotational velocity ($v \sin i$), the surface gravity ($\log(g)$) and the radial velocity (v_r) of the star.

TABLE 3
AVERAGE PARAMETERS FOR ALL STARS IN NGC 1333

ObjID	v_r [km s^{-1}]	σ	$v \sin i$ [km s^{-1}]	σ	$T_{\rm eff}$ [K]	σ	$\log g$ [$\log_{10}$ cm s^{-2}]	σ	r_H	σ	absJ [mag]	nobs	ngood[a]	var[b]
1	-27.80	0.43	92.94	0.68	6100	20	3.69	0.02	0.15	0.01	2.10	7	4	0
2	9.75	0.10	6.23	0.60	3540	10	3.98	0.03	0.11	0.01	4.50	7	6	0
4	-9.85	2.79	81.74	4.13	6570	30	3.38	0.07	0.33	0.05	3.60	7	6	0
5	$\cdots$	$\cdots$	$\cdots$	$\cdots$	$\cdots$	$\cdots$	$\cdots$	$\cdots$	$\cdots$	$\cdots$	$\cdots$	3	0	0
8	$\cdots$	$\cdots$	$\cdots$	$\cdots$	$\cdots$	$\cdots$	$\cdots$	$\cdots$	$\cdots$	$\cdots$	$\cdots$	3	0	0
10	9.38	0.27	27.81	0.45	3320	10	3.90	0.04	0.17	0.02	5.60	7	7	0
11	8.39	0.26	53.68	0.40	3760	10	3.64	0.02	0.12	0.01	3.20	7	6	0
12	9.29	0.09	11.94	0.26	3900	10	4.21	0.02	0.13	0.01	4.00	7	7	0
13	$\cdots$	$\cdots$	$\cdots$	$\cdots$	$\cdots$	$\cdots$	$\cdots$	$\cdots$	$\cdots$	$\cdots$	$\cdots$	3	0	0
17	$\cdots$	$\cdots$	$\cdots$	$\cdots$	$\cdots$	$\cdots$	$\cdots$	$\cdots$	$\cdots$	$\cdots$	$\cdots$	2	0	0
18	9.79	0.95	23.02	1.70	3270	30	3.77	0.13	0.22	0.07	4.10	7	2	0
19	9.81	0.68	58.26	1.06	4250	20	3.68	0.04	0.50	0.03	2.60	4	4	0
20	6.82	0.46	24.65	0.65	3030	20	2.81	0.05	0.29	0.05	3.40	1	1	0
22	7.88	0.57	17.79	1.12	2710	30	3.58	0.18	0.10	0.05	6.10	7	3	0
23	7.77	0.34	26.70	0.52	3440	20	3.27	0.05	0.19	0.02	3.20	1	1	0
24	$\cdots$	$\cdots$	$\cdots$	$\cdots$	$\cdots$	$\cdots$	$\cdots$	$\cdots$	$\cdots$	$\cdots$	$\cdots$	3	0	0
25	$\cdots$	$\cdots$	$\cdots$	$\cdots$	$\cdots$	$\cdots$	$\cdots$	$\cdots$	$\cdots$	$\cdots$	$\cdots$	3	0	0
28	6.29	0.47	21.24	0.88	3340	10	3.69	0.08	0.38	0.05	4.50	5	5	0
29	8.30	0.36	17.62	0.70	2880	20	3.77	0.14	0.02	0.03	4.30	1	1	0
33	11.07	0.67	34.42	1.17	3670	20	3.84	0.07	0.15	0.03	3.20	2	2	0
34	7.37	0.21	16.78	0.40	3170	10	3.12	0.03	0.74	0.04	2.50	3	2	1
35	7.80	1.14	24.99	2.08	3090	40	3.68	0.22	0.15	0.09	5.80	1	1	0
37	8.36	0.10	15.92	0.26	4310	10	4.34	0.02	0.31	0.01	3.10	7	6	0
39	7.80	1.06	26.03	1.69	2600	40	3.05	0.22	0.00	0.02	5.90	1	1	0
40	7.61	0.14	13.08	0.37	3620	10	3.87	0.03	0.23	0.02	4.10	5	5	0
41	6.72	1.37	25.02	2.59	2940	40	3.92	0.25	0.08	0.08	6.30	2	1	0
42	9.85	0.47	15.63	1.14	3740	40	3.82	0.09	0.31	0.04	2.70	4	2	0
43	7.50	0.58	15.52	1.03	3050	20	3.75	0.19	0.07	0.05	5.00	1	1	0
44	8.92	0.23	10.74	0.68	3750	20	3.83	0.05	0.62	0.04	3.10	1	1	0
48	8.13	0.38	14.09	0.91	3690	20	3.82	0.08	0.23	0.04	4.10	1	1	0
50	8.43	0.71	18.12	1.45	2780	80	3.43	0.56	0.01	0.07	5.80	1	1	0
51	8.16	0.59	9.79	1.84	3500	40	3.83	0.14	0.20	0.08	3.30	1	1	0
52	8.36	0.32	17.62	0.79	4130	30	4.27	0.06	0.89	0.03	2.70	1	1	0
56	9.08	0.30	7.94	1.26	3900	30	4.05	0.08	0.35	0.04	3.60	1	1	0
58	-309.02	41.27	463.52	77.24	3010	400	-0.27	0.75	0.33	0.37	6.10	1	1	0
59	$\cdots$	$\cdots$	$\cdots$	$\cdots$	$\cdots$	$\cdots$	$\cdots$	$\cdots$	$\cdots$	$\cdots$	$\cdots$	5	0	0
60	7.40	0.30	17.89	0.70	3460	20	3.86	0.06	0.10	0.03	3.90	1	1	0
61	7.38	0.40	10.11	1.11	3310	10	3.96	0.09	0.32	0.05	4.80	1	1	0
62	6.13	0.86	22.20	1.23	3920	30	3.96	0.07	0.00	0.00	4.60	1	1	0
63	9.83	0.18	16.43	0.44	4170	10	4.26	0.04	0.13	0.01	2.50	7	7	0
65	$\cdots$	$\cdots$	$\cdots$	$\cdots$	$\cdots$	$\cdots$	$\cdots$	$\cdots$	$\cdots$	$\cdots$	$\cdots$	2	0	0
66	98.00	28.27	78.82	32.89	3660	460	3.58	0.95	2.20	1.65	3.30	1	1	0
71	8.69	0.70	20.01	1.61	4540	100	4.32	0.15	0.26	0.06	0.40	1	1	0
74	4.98	3.28	23.09	9.04	3820	110	5.35	0.33	3.07	0.50	3.70	1	1	0
76	8.71	0.30	21.43	0.67	4020	10	4.26	0.05	0.12	0.02	4.70	2	2	0
77	7.34	1.01	42.77	1.57	3120	10	3.49	0.09	0.11	0.05	5.00	1	1	0
78	10.91	1.53	16.31	3.37	3560	110	3.52	0.26	0.19	0.13	3.00	1	1	0
79	$\cdots$	$\cdots$	$\cdots$	$\cdots$	$\cdots$	$\cdots$	$\cdots$	$\cdots$	$\cdots$	$\cdots$	$\cdots$	3	0	0
81	-226.61	1542.90	587.08	1292.89	2660	950	2.01	4.50	0.17	12.00	5.30	1	1	0
86	-1.14	0.32	10.65	1.07	3770	30	4.70	0.10	0.15	0.03	5.80	3	3	0
87	8.13	0.76	18.41	1.90	3570	30	3.89	0.11	1.30	0.13	4.80	2	2	0
91	$\cdots$	$\cdots$	$\cdots$	$\cdots$	$\cdots$	$\cdots$	$\cdots$	$\cdots$	$\cdots$	$\cdots$	$\cdots$	3	0	0
93	$\cdots$	$\cdots$	$\cdots$	$\cdots$	$\cdots$	$\cdots$	$\cdots$	$\cdots$	$\cdots$	$\cdots$	$\cdots$	2	0	0
94	8.82	0.56	33.07	1.07	4660	60	4.42	0.09	0.57	0.04	2.40	3	2	0
96	8.75	2.45	41.99	3.91	2960	40	3.69	0.26	0.01	0.05	6.20	1	1	0
97	9.26	0.29	34.15	0.52	3720	10	3.71	0.03	0.29	0.02	3.40	7	7	0
105	-47.24	366.32	483.26	606.64	4470	940	2.14	0.95	0.06	1.64	4.00	1	1	0
110	5.48	1.96	70.13	3.22	4010	50	3.33	0.09	0.45	0.07	1.50	1	1	0
111	$\cdots$	$\cdots$	$\cdots$	$\cdots$	$\cdots$	$\cdots$	$\cdots$	$\cdots$	$\cdots$	$\cdots$	$\cdots$	3	0	0
116	9.28	0.61	30.23	1.04	3930	20	4.00	0.06	0.25	0.03	2.80	1	1	0
118	9.07	0.69	19.61	1.41	3190	30	3.96	0.15	0.24	0.05	4.50	6	3	0
122	10.34	6.34	37.45	8.95	3430	170	3.46	0.56	0.93	0.51	3.60	1	1	0
125	-244.15	95.44	249.68	101.23	4500	370	2.03	0.40	0.02	0.22	10.10	1	1	0
127	$\cdots$	$\cdots$	$\cdots$	$\cdots$	$\cdots$	$\cdots$	$\cdots$	$\cdots$	$\cdots$	$\cdots$	$\cdots$	7	0	0
128	9.57	6.44	529.40	15.76	7000	0	3.85	0.04	0.18	0.03	1.20	1	1	0
130	7.24	0.57	69.18	0.76	5660	30	3.77	0.05	0.28	0.02	-0.60	3	1	0
131	9.47	1.85	15.71	3.73	3120	50	3.62	0.41	0.32	0.21	5.30	1	1	0
133	31.02	6.47	251.07	9.05	5950	60	4.01	0.09	0.17	0.04	4.10	7	7	0
136	$\cdots$	$\cdots$	$\cdots$	$\cdots$	$\cdots$	$\cdots$	$\cdots$	$\cdots$	$\cdots$	$\cdots$	$\cdots$	4	0	0
137	7.85	1.18	20.54	2.04	2620	50	3.82	0.50	0.00	0.02	5.60	1	1	0
138	8.33	1.48	21.13	2.53	3100	40	3.69	0.29	0.23	0.13	5.00	1	1	0
140	25.41	75.87	2.09	184.63	1900	1030	5.25	4.16	3.34	9.86	6.40	1	1	0
145	6.32	0.55	22.76	0.84	2970	20	3.88	0.13	0.01	0.02	5.70	3	3	0

TABLE 3 — *Continued*

ObjID	v_r [km s^{-1}]	σ	$v \sin i$ [km s^{-1}]	σ	$T_{\rm eff}$ [K]	σ	log g [log$_{10}$ cm s^{-2}]	σ	r_H	σ	absJ [mag]	nobs	ngood[a]	var[b]
152	$\cdots$	$\cdots$	$\cdots$	$\cdots$	$\cdots$	$\cdots$	$\cdots$	$\cdots$	$\cdots$	$\cdots$	$\cdots$	3	0	0
158	$\cdots$	$\cdots$	$\cdots$	$\cdots$	$\cdots$	$\cdots$	$\cdots$	$\cdots$	$\cdots$	$\cdots$	$\cdots$	2	0	0
159	8.47	0.30	20.61	0.65	3490	10	4.06	0.05	0.20	0.02	4.10	3	3	0
160	6.86	0.10	19.86	0.19	3310	0	3.79	0.02	0.17	0.01	4.20	7	7	0
162	$\cdots$	$\cdots$	$\cdots$	$\cdots$	$\cdots$	$\cdots$	$\cdots$	$\cdots$	$\cdots$	$\cdots$	$\cdots$	3	0	0
163	$\cdots$	$\cdots$	$\cdots$	$\cdots$	$\cdots$	$\cdots$	$\cdots$	$\cdots$	$\cdots$	$\cdots$	$\cdots$	3	0	0
167	8.07	0.17	13.49	0.42	3900	10	4.07	0.03	0.33	0.02	4.20	1	1	0
168	25.95	2.91	478.22	7.25	7000	0	3.99	0.02	0.70	0.02	0.90	3	3	1
171	8.13	0.69	33.74	1.39	4650	80	4.62	0.11	0.88	0.06	2.50	7	6	0
173	10.31	6.16	31.65	9.85	2960	150	4.00	1.04	0.23	0.35	5.80	1	1	0
174	7.54	0.26	17.94	0.49	3070	10	3.59	0.06	0.04	0.02	5.20	5	3	0
175	6.73	0.40	46.92	0.76	4200	10	4.38	0.03	1.02	0.02	3.10	7	6	1
176	1.22	3.27	121.79	4.23	3330	30	4.06	0.14	0.18	0.05	4.70	1	1	0
178	6.59	0.17	12.33	0.43	3120	10	3.51	0.04	0.34	0.03	5.00	2	2	0
179	6.78	0.36	14.67	0.83	3120	10	3.73	0.11	0.23	0.05	5.80	2	2	0
180	7.56	0.23	14.69	0.56	3690	10	3.98	0.04	0.01	0.00	4.60	4	4	1
181	9.05	0.76	26.63	1.16	3240	30	3.93	0.08	0.13	0.04	5.70	3	2	0
182	$\cdots$	$\cdots$	$\cdots$	$\cdots$	$\cdots$	$\cdots$	$\cdots$	$\cdots$	$\cdots$	$\cdots$	$\cdots$	2	0	0
183	$\cdots$	$\cdots$	$\cdots$	$\cdots$	$\cdots$	$\cdots$	$\cdots$	$\cdots$	$\cdots$	$\cdots$	$\cdots$	7	0	0
185	8.84	0.42	36.87	0.96	5250	50	4.81	0.07	0.55	0.04	2.30	2	2	0
186	7.25	0.22	14.94	0.50	3950	10	4.13	0.04	0.23	0.02	3.30	3	2	0
188	7.14	0.27	27.96	0.44	2610	10	2.93	0.03	0.00	0.00	6.20	7	7	0
189	6.85	0.11	9.52	0.41	4150	10	4.32	0.03	0.10	0.01	4.10	5	5	0
190	8.61	0.12	14.61	0.28	3310	0	3.78	0.03	0.18	0.01	4.50	7	7	1
191	7.01	0.13	9.53	0.42	3310	10	3.62	0.04	0.26	0.02	4.80	2	2	0
192	8.12	0.76	16.30	1.63	2930	30	4.11	0.19	0.03	0.06	6.30	2	1	0
193	5.82	0.27	19.73	0.49	3090	10	3.61	0.05	0.52	0.03	4.90	7	7	0
195	8.64	0.39	16.61	0.79	3190	20	3.96	0.08	0.23	0.03	5.90	5	4	0
197	7.26	0.08	9.84	0.26	3460	10	3.98	0.02	0.14	0.01	4.80	7	7	0
198	17.05	0.17	7.64	0.68	6710	30	5.22	0.04	0.11	0.02	2.80	7	7	0
199	7.60	0.59	21.58	1.06	2600	30	3.71	0.19	0.04	0.03	7.00	7	3	0
201	6.79	0.26	31.32	0.42	3120	10	3.96	0.03	0.10	0.01	5.30	7	6	0
202	2.99	1.16	9.78	4.00	3390	60	4.74	0.39	0.54	0.15	7.50	3	1	0
203	7.32	0.12	13.80	0.27	3140	0	3.43	0.03	0.71	0.02	4.40	7	7	0
204	7.71	0.13	21.60	0.24	3580	10	3.77	0.02	0.14	0.01	4.80	7	7	0

NOTE. — Table 3 will be published electronically. Fit parameters are the effective temperature ($T_{\rm eff}$), the veiling (r_H), the rotational velocity ($v \sin i$), the surface gravity (log(g)) and the radial velocity (v_r) of the star.

[a] Number of spectra meeting the quality criteria given in the text.

[b] Binary flag indicating if the source has a significantly variable radial velocity as defined in the text (1 for variable, 0 for non-variable).